JCI The Journal of Clinical Investigation

Frataxin deficiency promotes endothelial senescence in pulmonary hypertension

Miranda K. Culley, Jingsi Zhao, Yi Yin Tai, Ying Tang, Dror Perk, Vinny Negi, Qiujun Yu, Chen-Shan C. Woodcock, Adam Handen, Gil Speyer, Seungchan Kim, Yen-Chun Lai, Taijyu Satoh, Annie M.M. Watson, Yassmin Al Aaraj, John Sembrat, Mauricio Rojas, Dmitry Goncharov, Elena A. Goncharova, Omar F. Khan, Daniel G. Anderson, James E. Dahlman, Aditi U. Gurkar, Robert Lafyatis, Ahmed U. Fayyaz, Margaret M. Redfield, Mark T. Gladwin, Marlene Rabinovitch, Mingxia Gu, Thomas Bertero, Stephen Y. Chan

J Clin Invest. 2021;131(11):e136459. https://doi.org/10.1172/JCI136459.

Research Article **Pulmonology** **Vascular biology**

Graphical abstract

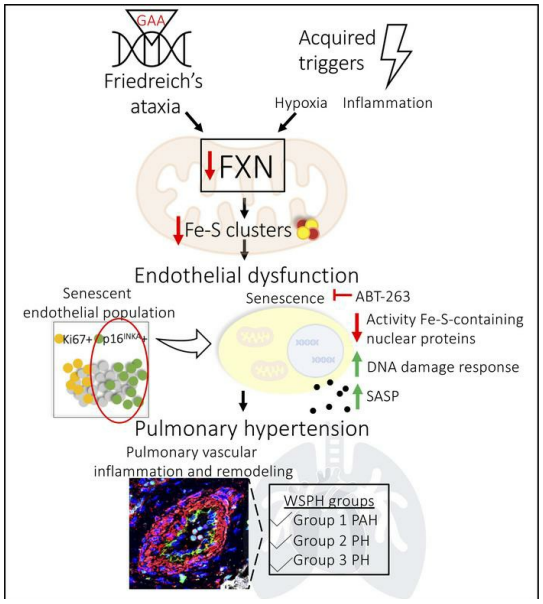

Find the latest version:

https://jci.me/136459/pdf

Frataxin deficiency promotes endothelial senescence in pulmonary hypertension

Miranda K. Culley,[1] Jingsi Zhao,[1] Yi Yin Tai,[1] Ying Tang,[1] Dror Perk,[1] Vinny Negi,[1] Qiujun Yu,[1,2] Chen-Shan C. Woodcock,[1] Adam Handen,[1] Gil Speyer,[3] Seungchan Kim,[4] Yen-Chun Lai,[5] Taijyu Satoh,[1] Annie M.M. Watson,[1] Yassmin Al Aaraj,[1] John Sembrat,[1] Mauricio Rojas,[6] Dmitry Goncharov,[7] Elena A. Goncharova,[7] Omar F. Khan,[8] Daniel G. Anderson,[9,10] James E. Dahlman,[11] Aditi U. Gurkar,[12] Robert Lafyatis,[1] Ahmed U. Fayyaz,[13,14] Margaret M. Redfield,[13] Mark T. Gladwin,[1] Marlene Rabinovitch,[15] Mingxia Gu,[16] Thomas Bertero,[17] and Stephen Y. Chan[1]

[1]Center for Pulmonary Vascular Biology and Medicine, Pittsburgh Heart, Lung, Blood Vascular Medicine Institute, Divisions of Cardiology, Pulmonary, Allergy, and Critical Care Medicine and Rheumatology, Department of Medicine, University of Pittsburgh School of Medicine and University of Pittsburgh Medical Center, Pittsburgh, Pennsylvania, USA. [2]University of Iowa Carver College of Medicine, Iowa City, Iowa, USA. [3]Research Computing, Arizona State University, Tempe, Arizona, USA. [4]Center for Computational Systems Biology, Department of Electrical and Computer Engineering, College of Engineering, Prairie View A&M University, Prairie View, Texas, USA. [5]Division of Pulmonary, Critical Care, Sleep and Occupational Medicine, Indiana University School of Medicine, Indianapolis, Indiana, USA. [6]Division of Pulmonary, Critical Care, and Sleep Medicine, Department of Medicine, Ohio State University College of Medicine, Columbus, Ohio, USA. [7]Lung Center, Pulmonary Vascular Disease Program, Division of Pulmonary, Critical Care and Sleep Medicine, University of California Davis School of Medicine, Davis, California, USA. [8]Institute of Biomedical Engineering, Department of Immunology, University of Toronto, Toronto, Ontario, Canada. [9]Department of Chemical Engineering, Institute of Medical Engineering and Science, Harvard-MIT Division of Health Sciences & Technology, Massachusetts Institute of Technology, Cambridge, Massachusetts, USA. [10]David H. Koch Institute for Integrative Cancer Research, Massachusetts Institute of Technology, Cambridge, Massachusetts, USA. [11]Wallace H. Coulter Department of Biomedical Engineering, Georgia Institute of Technology, Atlanta, Georgia, USA. [12]Aging Institute, Division of Geriatric Medicine, University of Pittsburgh School of Medicine and University of Pittsburgh Medical Center, GRECC VA, Pittsburgh, Pennsylvania, USA. [13]Department of Cardiovascular Medicine and [14]Department of Laboratory Medicine & Pathology, Mayo Clinic, Rochester, Minnesotta, USA. [15]Department of Pediatrics, Stanford University School of Medicine, Stanford, California, USA. [16]Perinatal Institute, Division of Pulmonary Biology Center for Stem Cell and Organoid Medicine, CuSTOM, Division of Developmental Biology, Department of Pediatrics, Cincinnati Children's Hospital Medical Center, University of Cincinnati, Cincinnati, Ohio, USA. [17]Université Côte d'Azur, CNRS, UMR7275, IPMC, Valbonne, France.

The dynamic regulation of endothelial pathophenotypes in pulmonary hypertension (PH) remains undefined. Cellular senescence is linked to PH with intracardiac shunts; however, its regulation across PH subtypes is unknown. Since endothelial deficiency of iron-sulfur (Fe-S) clusters is pathogenic in PH, we hypothesized that a Fe-S biogenesis protein, frataxin (FXN), controls endothelial senescence. An endothelial subpopulation in rodent and patient lungs across PH subtypes exhibited reduced FXN and elevated senescence. In vitro, hypoxic and inflammatory FXN deficiency abrogated activity of endothelial Fe-S–containing polymerases, promoting replication stress, DNA damage response, and senescence. This was also observed in stem cell–derived endothelial cells from Friedreich's ataxia (FRDA), a genetic disease of FXN deficiency, ataxia, and cardiomyopathy, often with PH. In vivo, FXN deficiency–dependent senescence drove vessel inflammation, remodeling, and PH, whereas pharmacologic removal of senescent cells in Fxn-deficient rodents ameliorated PH. These data offer a model of endothelial biology in PH, where FXN deficiency generates a senescent endothelial subpopulation, promoting vascular inflammatory and proliferative signals in other cells to drive disease. These findings also establish an endothelial etiology for PH in FRDA and left heart disease and support therapeutic development of senolytic drugs, reversing effects of Fe-S deficiency across PH subtypes.

Introduction

Pulmonary hypertension (PH) is a fatal disease of the lung vasculature with incompletely defined molecular underpinnings (1, 2). Our understanding of disease pathophysiology as well as existing treatments are largely exclusive to the most severe subtype, Group 1 pulmonary arterial hypertension (PAH), as defined by the World Symposium on Pulmonary Hypertension (WSPH) (1). Notably, as the population ages and the number of patients with chronic diseases rises (3), PH due to left heart disease (Group 2), particularly PH associated with heart failure with preserved ejection fraction (HFpEF) (4) and metabolic syndrome (5), and PH due to hypoxic lung disease (Group 3) (6) represent a majority of PH patients with limited treatments available. How the molecular mechanisms that underlie PAH and other PH groups are connected is still under investigation.

Pulmonary endothelial dysfunction is a defining feature of vascular remodeling in PAH but is less defined across PH subtypes. While many postulate the endothelium as the site of inciting injury and apoptosis followed by hyperproliferation (7), endothelial cells exhibit dynamic, spatio-temporal phenotypes that are not

▶ Related Commentary: https://doi.org/10.1172/JCI149721

Conflict of interest: SYC has served as a consultant for United Therapeutics. SYC is a director, officer, and shareholder in Synhale Therapeutics. SYC has held grants from Actelion and Pfizer. SYC and TB have filed patent applications regarding metabolism in pulmonary hypertension (US 10,925,869 B2, "Compositions and methods for treating pulmonary vascular disease" and WO 2015/171641 A1, "Coordinate control of pathogenic signaling by the MIR-130-301 family in pulmonary hypertension and fibroproliferative diseases").

Submitted: January 21, 2020; **Accepted:** April 22, 2021; **Published:** June 1, 2021.
Reference information: *J Clin Invest*. 2021;131(11):e136459.
https://doi.org/10.1172/JCI136459.

yet fully understood. Important in the pathology of peripheral vascular beds (8), senescence is one alternative endothelial fate that is a state of stable growth arrest defined by upregulation of markers like *CDKN2A*/p16^{INK4} and senescence-associated β-galactosidase (SA-β-gal). While this pathophenotype has been linked to PAH due to congenital heart disease (9) or chronic lung disease (10), its relevance in other WSPH groups is unclear (11). Notably, senescent cells undergo morphologic, genomic, and metabolic reprogramming and produce an assembly of pathogenic molecules (e.g., cytokines), referred to as the senescence-associated secretory phenotype (SASP) (12), that propagates underlying tissue inflammation and altered regenerative capacity (13). In cancer and diseases of aging, multiple aberrant cellular processes converge to drive senescence, including attenuated mitochondrial metabolism and genomic integrity (14). Addressing the latter, pathological DNA breaks develop in response to several extrinsic and intrinsic factors such as products of metabolism (e.g., oxidative stress) or replication stress (e.g., error-prone replication fork progression) (15), and, in turn, lead to the DNA damage response (DDR), a multistep process that detects damage and signals for DNA repair (16). If the repair machinery is compromised or overwhelmed by the causative agents of endogenous DNA damage, cell-fate outcomes vary between apoptosis and DDR-dependent senescence (17, 18). While genotoxic stress (19–23) has been observed in patients with PH, the complex regulatory events that control endothelial senescence and how such events fit into the development of pulmonary vascular inflammation and remodeling are not known.

We previously demonstrated that endothelial iron-sulfur (Fe-S) cluster deficiency disrupts mitochondrial function and promotes PH development (24–26). Fe-S clusters are essential cofactors for processes like oxidative phosphorylation (27) and DNA replication and repair (28, 29). The synthesis, trafficking, and integration of these bioinorganic cofactors require many mitochondrial and cytoplasmic assembly proteins (28–30), and their importance in human disease has been reinforced by reports of patients with mutations in iron sulfur assembly proteins 1 and 2 (ISCU1/2) (25, 31), BOLA3 (32), and NFU1 (33, 34), who also exhibit PH. Our prior work demonstrated how hypoxia-inducible factor alpha (HIF-α), a transcription factor involved in metabolic rewiring in PH (35, 36), acts as a master regulator of endothelial ISCU1/2 and BOLA3 levels (24, 26). Moreover, both genetic and acquired deficiencies of ISCU1/2 or BOLA3 resulted in Fe-S–dependent metabolic rewiring, which induced endothelial dysfunction and PH in vivo (24–26). Notably, other vascular cell types with Fe-S deficiencies, such as smooth muscle cells, did not manifest similar phenotypes (25). This may be a consequence of differences in mitochondria or absolute Fe-S clusters across cell types, emphasizing the importance of endothelial Fe-S biology. Whether deficiencies of other Fe-S assembly genes and their genotoxic rather than metabolic consequences play a mechanistic role in PH pathogenesis is unclear.

Frataxin (FXN) is a mitochondrial binding partner of ISCU1/2 and iron chaperone essential to Fe-S biogenesis (37, 38). Both elevated (39, 40) and reduced (41) FXN levels have been reported in different hypoxic cell types, but the interaction of FXN and hypoxia, as well as other acquired PH triggers, in pulmonary vascular cells remains largely uncharacterized. Instead, FXN has been predominantly studied in the context of genetic deficiency: homozygous GAA trinucleotide repeat mutations lead to decreased FXN, causing Friedreich's ataxia (FRDA) (42). This multisystem disease is defined by neurodegeneration and hypertrophic cardiomyopathy (and less often dilated cardiomyopathy, ref. 43) with the latter driving mortality in roughly 60% of patients (44). Pulmonary arteriolar vasculopathy has been reported in this population (45), consistent with the fact that up to 40% of patients with hypertrophic cardiomyopathy (HCM) in general suffer from Group 2 PH (46, 47). Yet, PH and cardiopulmonary complications in FRDA have been surprisingly underreported (48, 49), due to the lack of hemodynamic outcomes and lung specimens available for study. Instead, the focus has been on cardiomyocyte dysfunction and markedly elevated left ventricular filling pressures rather than the PH that, by definition, is present (49). Furthermore, since FRDA-dependent FXN deficiency in nonvascular cell types can drive DNA damage (50, 51), arrested growth and apoptosis (52), and senescence (53), it is plausible that these same phenotypes in endothelial cells could have profound pathobiological consequences. Thus, we investigated if endothelial FXN deficiency, due to either genetic or acquired triggers, controls Fe-S–mediated senescence, thus driving key pathophenotypes not only in PAH but also in more poorly understood PH subtypes.

Results

Decreased FXN and increased senescence in pulmonary endothelial cells in PH. To determine whether cellular senescence develops in FXN-deficient endothelial cells in PH, we quantified vascular expression of FXN and the senescence marker *CDKN2A*/p16^{INK4} (12) in multiple in vivo models of PH representing diverse clinical subtypes. Immunofluorescent confocal microscopy of the pulmonary vasculature (Figure 1A and Supplemental Figure 1, A and B; supplemental material available online with this article; https://doi.org/10.1172/JCI136459DS1) revealed a marked reduction in Fxn in the CD31$^+$ endothelium as well as the α-SMA$^+$ smooth muscle layer and pulmonary vessel in a monocrotaline rat model of Group 1 PAH (54). MCT lungs also displayed increased *Cdkn2a* transcripts (Figure 1B). Correspondingly, expression analysis of whole-lung tissue from transgenic mice expressing the inflammatory cytokine IL-6 in normoxic (Supplemental Figure 1C) or hypoxic (Supplemental Figure 1D) conditions, representing a second hit to model Group 1 PAH (55), displayed reduced *Fxn* (Figure 1C). Emphasizing endothelial-specific deficiency, isolated CD31$^+$ endothelial cells from the lungs of hypoxic IL-6 transgenic mice demonstrated *Fxn* downregulation (Figure 1C). Importantly, lungs of this Group 1 PAH model exhibited increased *Cdkn2a* transcript when compared with normoxic wild-type controls (Figure 1D). Apart from Group 1 PAH, in lungs from obese ZSF1 rats exposed to the VEGF receptor antagonist SU-5416 (Ob-Su), a model of Group 2 PH due to heart failure with preserved ejection fraction (PH-HFpEF) (ref. 56 and Supplemental Table 1), Fxn (Figure 1E and Supplemental Figure 1E) was reduced, and *Cdkn2a* was increased (Figure 1F) compared with lean controls. Similarly, in human lung tissue, FXN levels were reduced in CD31$^+$ endothelium (Figure 1G) in patients with Group 1 PAH (Supplemental Table 2) as well as interstitial pulmonary fibrosis–associated (IPF-associated) PH (Group 3 PH) (Supplemental Table 3) as compared with nondiseased controls.

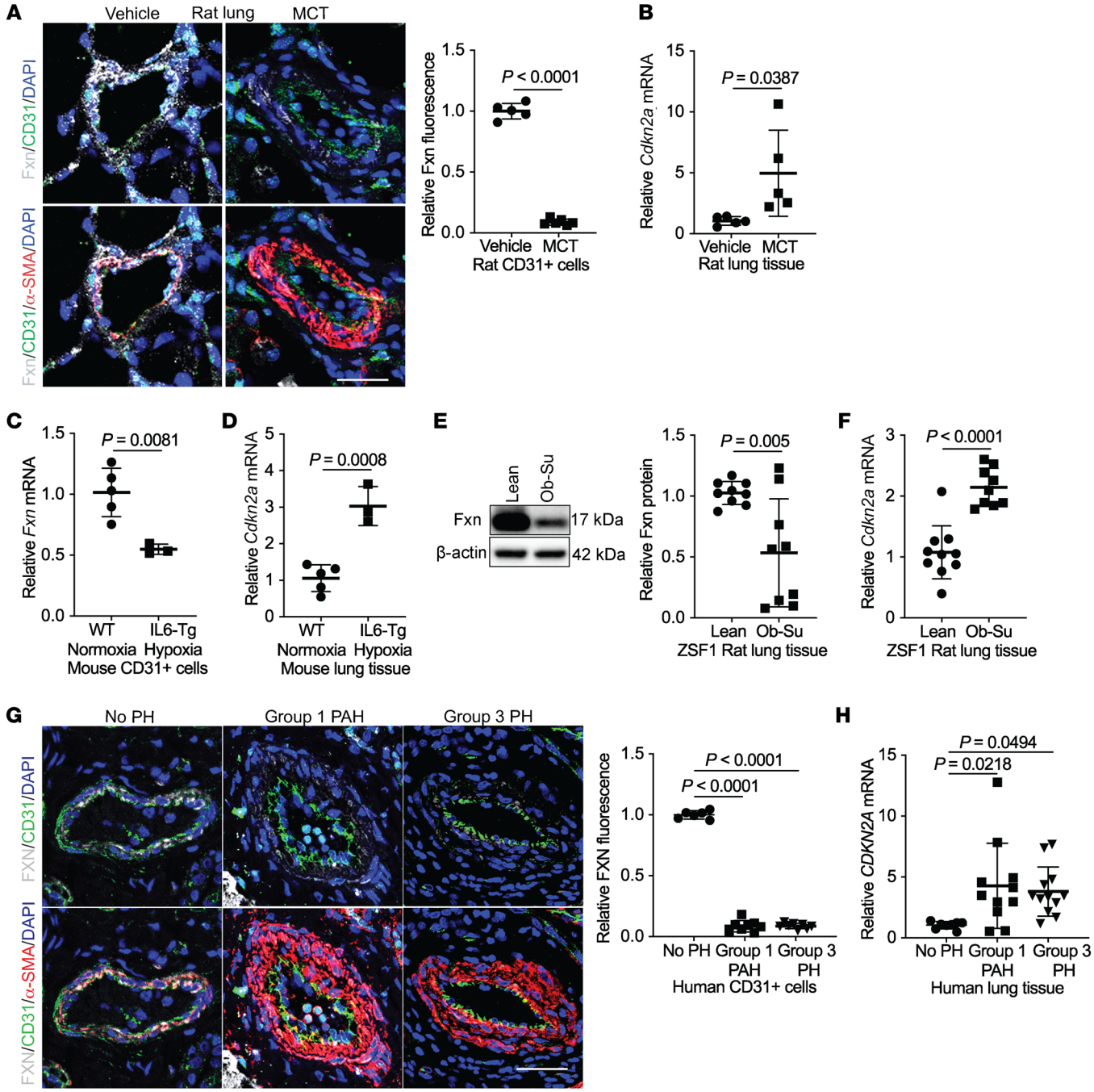

Figure 1. Reduced FXN and elevated *CDKN2A* expression in Group 1, 2, and 3 PH lungs. (**A**) Representative images of lungs stained with immunofluorescent probes for Fxn (gray), CD31 (green), α-SMA (red), counterstained with DAPI (blue), and imaged by confocal microscopy. Scale bar: 50 μm. Quantification of Fxn colocalized within the CD31⁺ endothelium in rats treated with monocrotaline (MCT) (n = 6) or vehicle (n = 5). (**B**) Relative *Cdkn2a* expression by RT-qPCR in lung tissue from MCT-treated rats compared with vehicle control (n = 5/group). (**C**) *Fxn* mRNA expression in isolated CD31⁺ cells and (**D**) whole-lung *CDKN2A* mRNA levels in hypoxic interleukin-6 transgenic (IL6-Tg) (n = 3) versus normoxic WT mice (n = 5). (**E**) Fxn protein and (**F**) *Cdkn2a* transcript expression in lung tissue from ZSF1 obese rats treated with Sugen (SU5416) (Ob-Su) (n = 9) versus lean controls (n = 9–10). (**G**) Representative confocal images showing FXN (gray), CD31 (green), α-SMA (red), and counterstained with DAPI (blue). Scale bar: 50 μm. Quantification of FXN in the CD31⁺ endothelium of Group 1 PAH (n = 8) or Group 3 PH (n = 8) patient lungs compared with controls (No PH) (n = 6). (**H**) RT-qPCR of *CDKN2A* mRNA levels in lung tissue of patient without PH (n = 8), Group 1 (n = 11), or Group 3 PH (n = 12). Two-tailed Student's t test (**A**–**F**) and 1-way ANOVA and Tukey's post hoc analysis (**G** and **H**) with error bars that reflect mean ± SD.

Of note, in these cases, FXN levels were also reduced in α-SMA⁺ smooth muscle layer (Supplemental Figure 1F). Conversely, *CDKN2A*/p16^{INK4} was increased in homogenized lung tissue (Figure 1H) of PH patients compared with controls, with distinct signal in the endothelium (Supplemental Figure 1G). Thus, endothelial FXN downregulation and *CDKN2A*/p16^{INK4} upregulation were consistently observed across rodent and human examples of PH subtypes. Moreover, because alterations in FXN

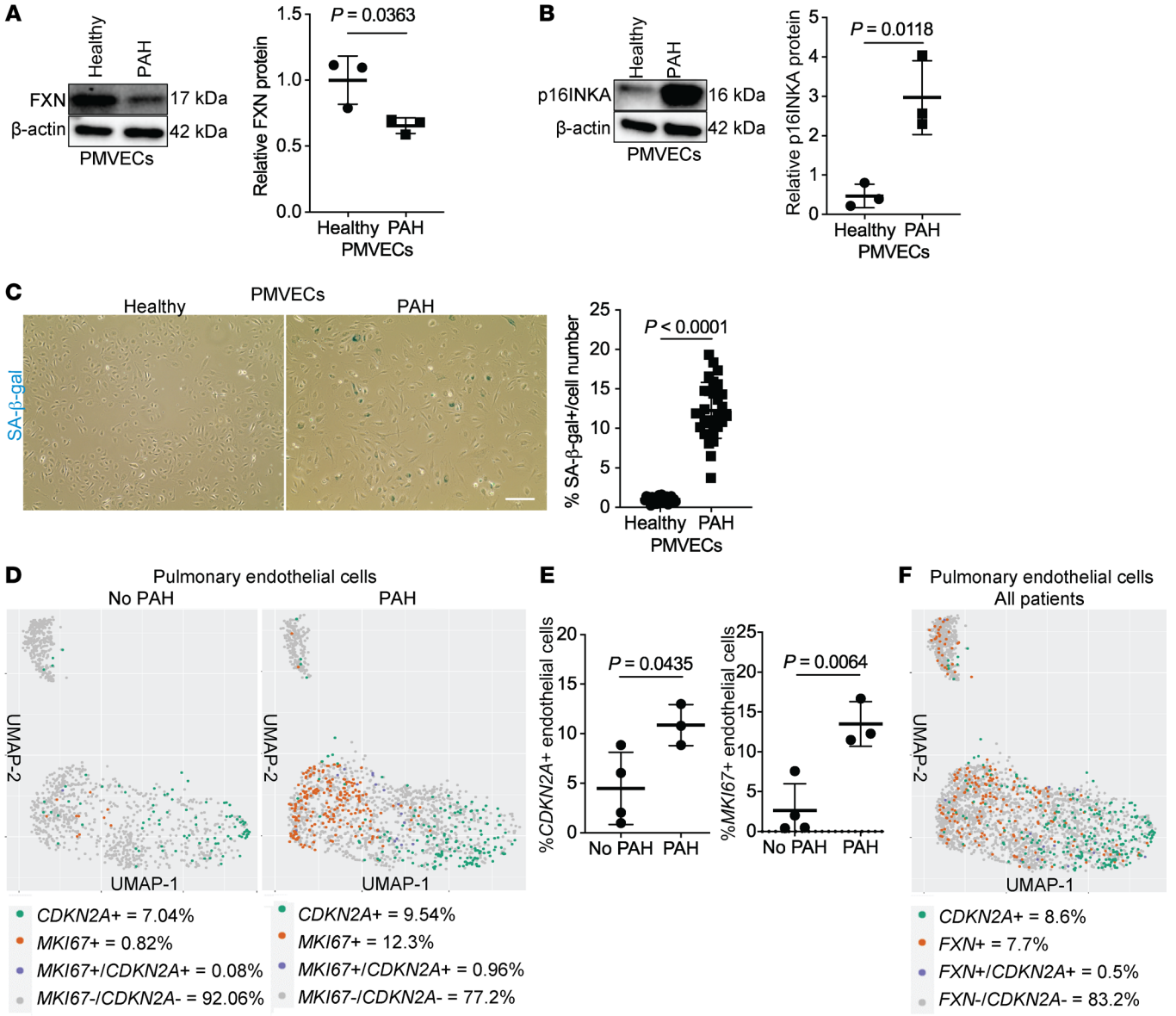

Figure 2. A subpopulation of FXN-deficient senescent cells in the endothelium of patients with PAH. (**A** and **B**) Immunoblot of FXN and p16^{INKA} levels in cultured pulmonary microvascular endothelial cells (PMVECs) from a healthy patient versus a Group 1 patient with PAH (n = 3/group). (**C**) Representative brightfield images (scale bar: 400 μm) and quantification of the percentage of SA-β-gal–positive PMVECs (blue) from a healthy patient versus a Group 1 patient with PAH. (**D**) From single-cell RNA sequencing of lungs from Group 1 patients with PAH (n = 3) versus no PAH control (n = 4), aggregate UMAP plots were generated of all endothelial cells in each cohort. Single-positive (*CDKN2A*, green or *MKI67*, orange), double-positive (blue), and double-negative (gray) endothelial cells are marked, along with total percentages across the aggregate cohort populations. (**E**) Percentages of *CDKN2A*-positive and *MKI67*-positive endothelial cells in each individual patient were compared between cohorts (PAH vs. no PAH). (**F**) Aggregate UMAP plot of pulmonary endothelial cells across all sampled patients (n = 7), demonstrating the percentage of single-positive (*CDKN2A*-expressing, green or high *FXN*-expressing, orange), double-positive (*CDKN2A*-expressing and high *FXN* expressing, blue), and double-negative (*CDKN2A*-expressing and non–high FXN expressing, gray) cells. Two-tailed Student's t test with error bars that reflect mean ± SD.

expression were not exclusive to the endothelium, these findings emphasized the need to define the functional consequences of FXN deficiency in endothelium versus other vascular cell types.

To specifically define the extent of endothelial senescence in PH, cultured human pulmonary microvascular ECs (PMVECs) from a PAH patient displayed decreased FXN (Figure 2A and Supplemental Figure 1H) versus an age- and sex-matched non-PAH control. Importantly, total p16^{INK4} and SA-β-gal staining were increased (Figure 2, B and C) in PAH-PMVECs. Importantly, only a subcohort of PAH cells stained SA-β-gal$^+$, indicating that senescence does not necessarily predominate across the entire endothelial population of this PAH patient. To determine whether senescent cells are distinct from other known endothelial phenotypic cohorts known to drive PH (i.e., proliferating endothelium), we analyzed single-cell RNA sequencing data from 3 human lungs of patients with PAH compared with 4 control patients without PAH (Supplemental Table 4 and ref. 57), matched for age and absence of senescence-altering medications. When comparing endothelial

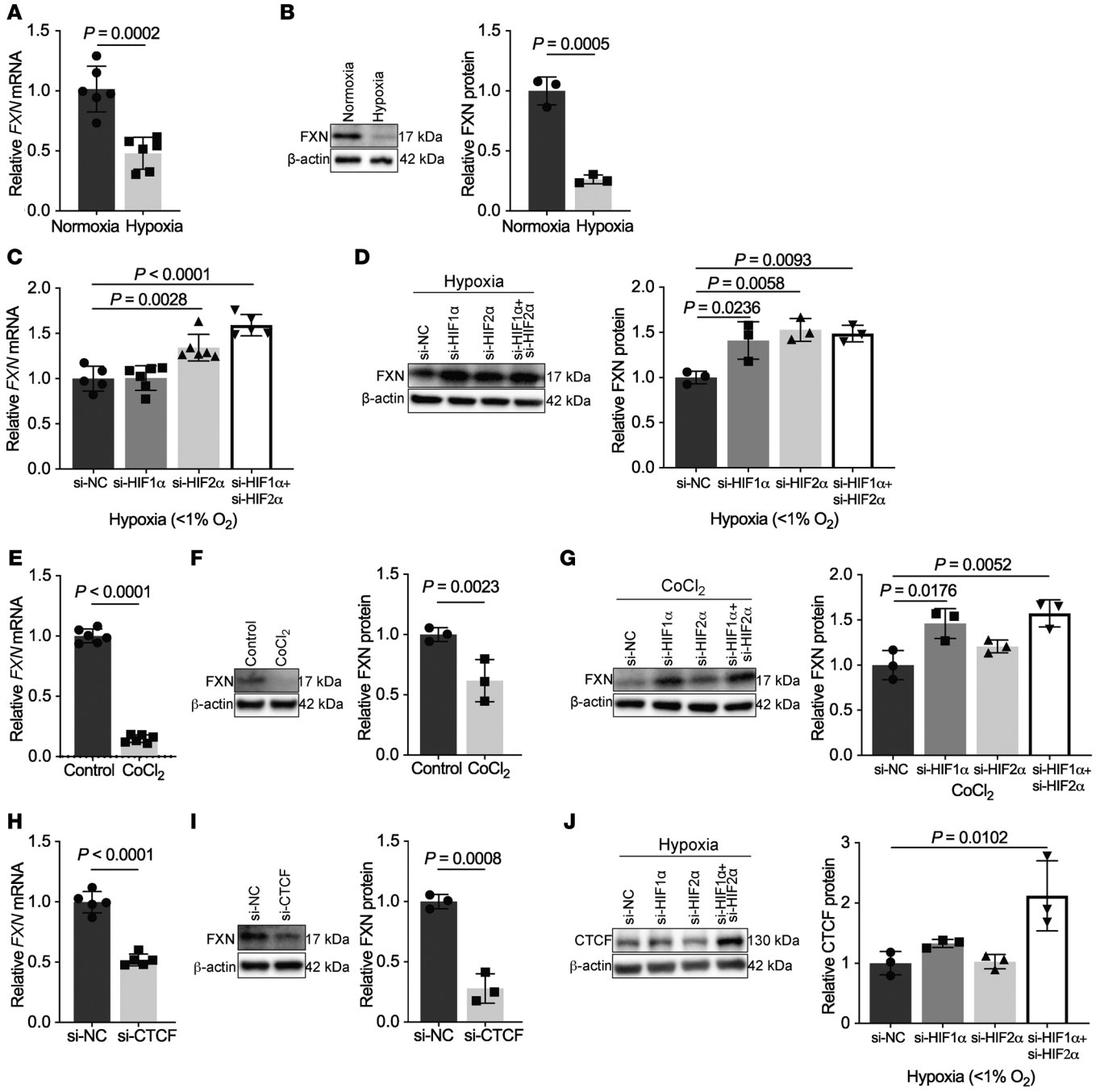

Figure 3. Hypoxia downregulates FXN expression via a HIF-α/CTCF axis in pulmonary artery endothelial cells. (**A** and **B**) RT-qPCR analysis (n = 6/group) and immunoblot with densitometry (n = 3/group) of FXN in cultured human pulmonary artery endothelial cells (PAECs) after exposure to hypoxia (≥ 24 hours, < 1% O_2). (**C** and **D**) Relative FXN transcript (n = 5–6/group) and protein levels (n = 3/group) in hypoxic PAECs transfected with HIF-1α, HIF-2α, or combined isoform-specific siRNAs compared with negative control (NC). (**E** and **F**) FXN expression analysis in PAECs treated with the HIF-1α activator cobalt(II) chloride (≥ 24 hours, 750 μM $CoCl_2$) (n = 6/group and n = 3/group). (**G**) Immunoblot of FXN in PAECs treated with $CoCl_2$ and transfected with HIF-1α, HIF-2α, or both siRNAs, compared with negative control (n = 3/group). (**H** and **I**) RT-qPCR (n = 5/group) and immunoblot (n = 3/group) of FXN in PAECs transfected with siRNA against CTCF or negative control. (**J**) Immunoblot of CTCF in hypoxic PAECs transfected with HIF-1α, HIF-2α, or both siRNAs, compared with control (n = 3/group). Two-tailed Student's t test (**A**, **B**, **E**, **F**, **H**, and **I**) and 1-way ANOVA and Tukey's post hoc analysis (**C**, **D**, **G**, and **J**) with error bars that reflect mean ± SD.

cells and using an expression cutoff that distinguished high (positive) versus low-to-negligible (negative) levels, mean percentages of senescent *CDKN2A*-positive and proliferating *MKI67*-positive cells were increased in endothelial cells in PAH lungs (Figure 2D) with only rare double-positive cells. Given the relatively low endogenous expression of *FXN* in endothelial cells, single-cell sequencing could only distinguish high *FXN*-expressing endothelial cells. Notably, cells displaying high FXN levels were consistently *CDKN2A*-negative, whereas *CDKN2A*-positive endothelial cells rarely displayed such high *FXN* levels (Figure 2E). Thus, we identified a cohort of

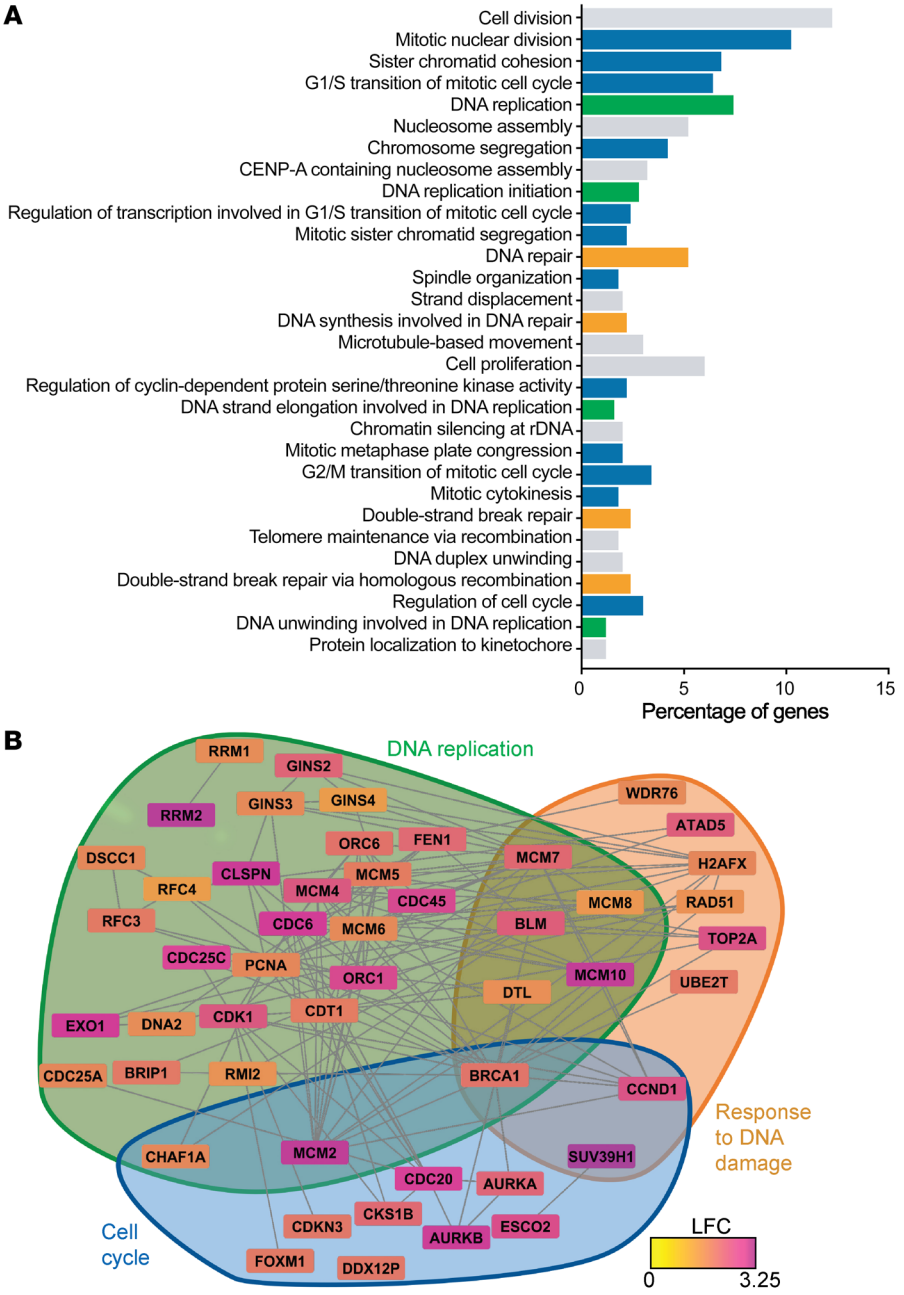

Figure 4. RNA sequencing of FXN-deficient pulmonary artery endothelial cells. (**A**) Long RNA sequencing in PAECs transfected with FXN siRNA versus negative control followed by GO enrichment (n = 3/group). Histogram of the top 30 most significant direct GO terms (log fold change [LFC] > 1.2, FDR < 0.05) representing the percentage of differentially expressed genes in the RNAseq data set within each pathway. GO terms specifically related to cell cycle (blue), DNA replication (green), and cellular response to DNA damage stimulus (orange) and others (gray). (**B**) Hypergraph of differentially expressed genes (FDR < 0.05), depicting log fold change via a color scale within GO pathways pertaining to cell cycle (blue), DNA replication (green), and cellular response to DNA damage stimulus (orange).

CDKN2A-positive senescent pulmonary endothelial cells without substantial FXN expression, distinct from proliferative endothelial cells in the same lung. Taken together, diverse rodent and human models across various PH groups exhibited a distinct subpopulation of pulmonary vascular endothelial $p16^{INK4}$-positive cells with reduced FXN, indicating a potential mechanistic link between FXN and senescence in Groups 1–3 PH.

HIF-α controls CTCF to downregulate endothelial FXN. To explore the mechanisms of dynamic FXN regulation in PH-specific contexts, human primary pulmonary vascular cells were exposed to known PH triggers. Exposure to hypoxia, a trigger associated with Group 1 PAH and Group 3 PH (6), robustly downregulated FXN transcript and protein levels in human pulmonary arterial endothelial cells (PAECs; Figure 3, A and B). Similarly, exposure to the inflammatory cytokines that are elevated (58) and promote vascular remodeling in Group 1 PAH (59), such as interleukin-1 beta (IL-1β), decreased FXN in PAECs (Supplemental Figure 2, A and B). Mirroring hypoxic IL-6 transgenic mice with decreased endothelial *Fxn* (Figure 1C), FXN was more robustly downregulated by a combination of hypoxia with IL-6 and its receptor than hypoxia alone (Supplemental Figure 2, C and D). Notably, hypoxia downregulated FXN in pulmonary artery smooth muscle cells (PASMCs) but not adventitial fibroblasts (PAAFs, Supplemental Figure 2E), while inflammation did not alter FXN in either cell type (Supplemental Figure 2F). Knockdown of genes associated with heritable PAH or exposure to increased matrix stiffness also did not alter FXN expression in PAECs (Supplemental Figure 2, G and H). Thus, hypoxic and inflammatory stimuli associated with Groups 1 and 3 PH specifically downregulated FXN in pulmonary endothelial cells.

Given the importance of HIF-α activity in Fe-S biogenesis (24–26), we aimed to determine whether hypoxic downregulation of FXN was dependent on HIF-α. PAECs were treated with siRNA specific for the HIF-α isoforms HIF-1α and HIF-2α, alone and in combination, followed by exposure to chronic hypoxia (Supplemental Figure 3, A and B). HIF-1α and HIF-2α knockdown together most effectively increased FXN (Figure 3, C and D) under hypoxic stimulus, particularly at the transcript level. Bolstering these results, the HIF-activator cobalt(II) chloride (60) robustly decreased FXN (Figure 3, E and F), whereas HIF-1α–specific inhibition by siRNA reversed this effect (Figure 3G). Inflammatory cytokines (such as IL-1b) are known to drive expression of HIF-α even under normoxic conditions (61), and more broadly, HIF-dependent processes are known to serve as an important stress response in inflammatory

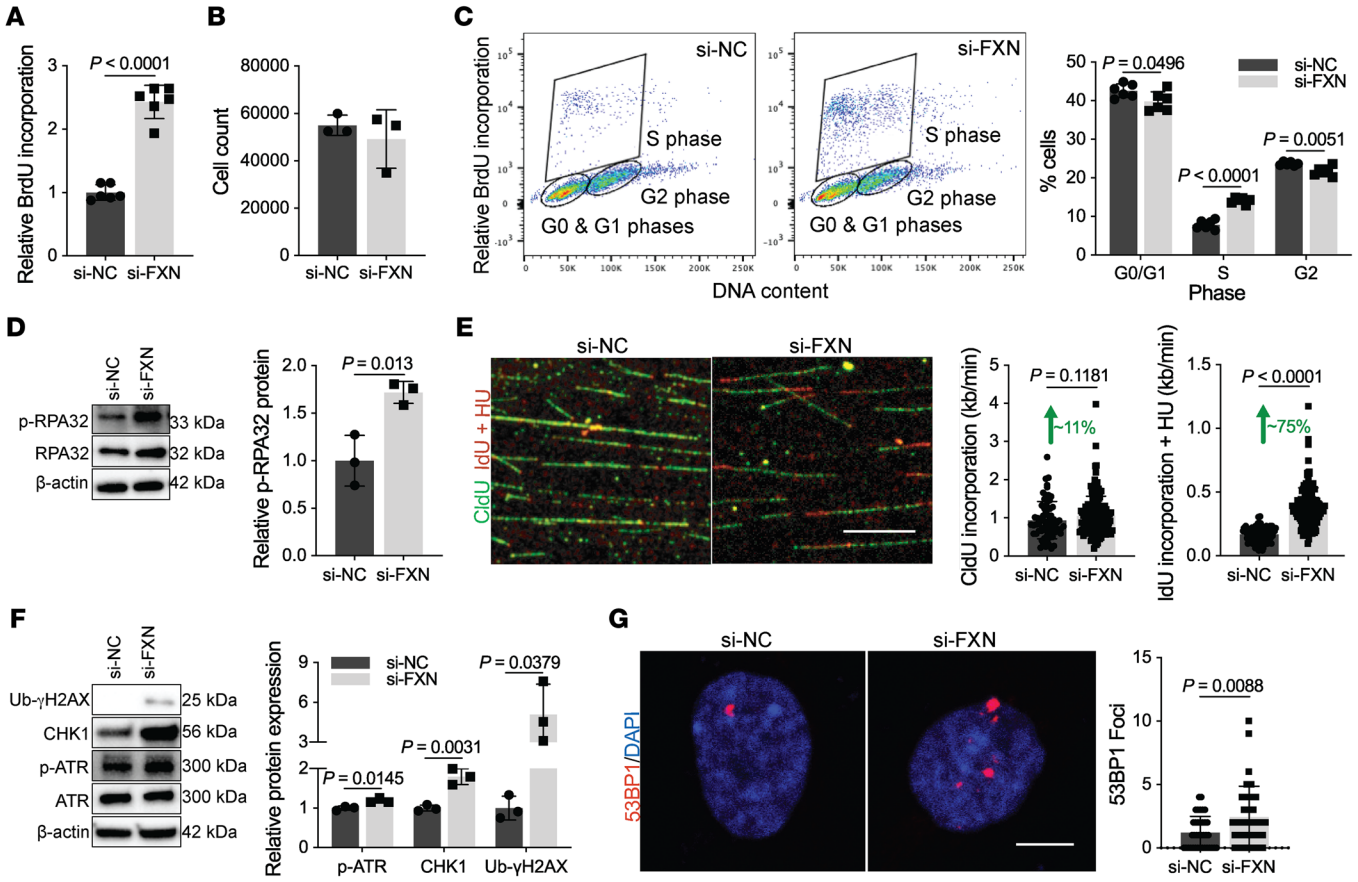

Figure 5. Acute FXN knockdown promotes replication stress and S-phase arrest. (**A**–**G**) All experiments were performed 48 hours after transfection in PAECs with or without FXN inhibition by siRNA. (**A**) Colorimetric BrdU incorporation (n = 6/group). (**B**) Manual PAEC count (n = 3/group). (**C**) Flow cytometric analysis of FXN-deficient or control PAECs pulsed with BrdU and the DNA marker 7-AAD (n = 6/group). (**D**) Immunoblot and quantification of the replication stress marker, phosphorylated RPA32 (p-RPA32) (n = 3/group). (**E**) Representative confocal imaging and quantification of replication rate (kb/min) in FXN-deficient or control PAECs pulsed with CldU (20 minutes, 50 μM; green) followed by IdU (20 minutes, 250 μM; red) with hydroxyurea (2 mM; HU) (n = 175 versus n = 204 forks). Scale bar: 10 μm. (**F**) Quantified immunoblot of DNA damage response markers (p-ATR, CHK1, Ub-γH2AX) (n = 3/group). (**G**) Immunofluorescence staining and confocal microscopy of nuclear 53BP1 foci (red) within DAPI-stained nuclei (blue) (n = 37 versus n = 34). Scale bar: 10 μm. Two-tailed Student's t test with error bars that reflect mean ± SD.

diseases (62). Reinforcing this idea, IL1-β–treated PAECs exhibited increased *HIF1A* transcript levels (Supplemental Figure 3C), suggesting HIF-driven FXN reduction may be a common mechanism across hypoxic and inflammatory triggers. Moreover, immunofluorescent labeling demonstrated increased expression of HIF-1α in obese, SU5416-treated rat lungs modeling Group 2 PH-HFpEF (Supplemental Figure 3D) and in Group 1 and 3 PH patient lungs (Supplemental Figure 3E), consistent with decreased FXN levels in these PH models (Figure 1). Altogether, despite the HIF-responsive element in the *FXN* promoter (39, 40), these data support the context-dependent, repressive activity of both HIF-α isoforms on FXN in hypoxic PAECs as well as in the lungs of multiple PH models.

Consistent with a prior description of the chromatin insulator protein CCCTC-binding factor (CTCF) binding the *FXN* 5′UTR (63), we found that CTCF inhibition by siRNA (Supplemental Figure 4A) markedly reduced FXN (Figure 3, H and I) in PAECs. We observed reduced CTCF protein following chronic hypoxic exposure (Supplemental Figure 4B) and cobalt(II) chloride treatment (Supplemental Figure 4C), consistent with FXN knockdown under these conditions (Figure 3, A, B, G, and H). Moreover, knockdown of the HIF-1α and HIF-2α isoforms together rescued CTCF (Figure 3J), corresponding with rescue of FXN levels (Figure 3, E and F). In sum, HIF-α controls CTCF-dependent epigenetic modulation of FXN expression in hypoxic PAECs.

To determine the pathologic relevance of this pathway, immunofluorescence staining was performed for CTCF in the lung vasculature of rodents and patients with PH. Along with HIF-1a upregulation (Supplemental Figure 3, C and D), obese rats treated with SU5416 (Supplemental Figure 4D) and patients with Group 1 PAH or Group 3 PH (Supplemental Figure 4E) exhibited decreased CTCF levels in their pulmonary vessels and specifically their pulmonary endothelium. In summary, these data highlight HIF-α–driven epigenetic silencing of FXN following exposure to hypoxia in vitro and suggest a shared mechanism in multiple PH subtypes.

Acute FXN knockdown promotes endothelial replication stress and cell cycle arrest. To confirm that our model of FXN deficiency in primary human pulmonary endothelial cells leads to alterations of Fe-S cluster levels, Fe-S integrity in PAECs was assessed using a fluorescent glutaredoxin 2 (GRX2) sensor, which homodimerizes and fluoresces in proportion to the level of

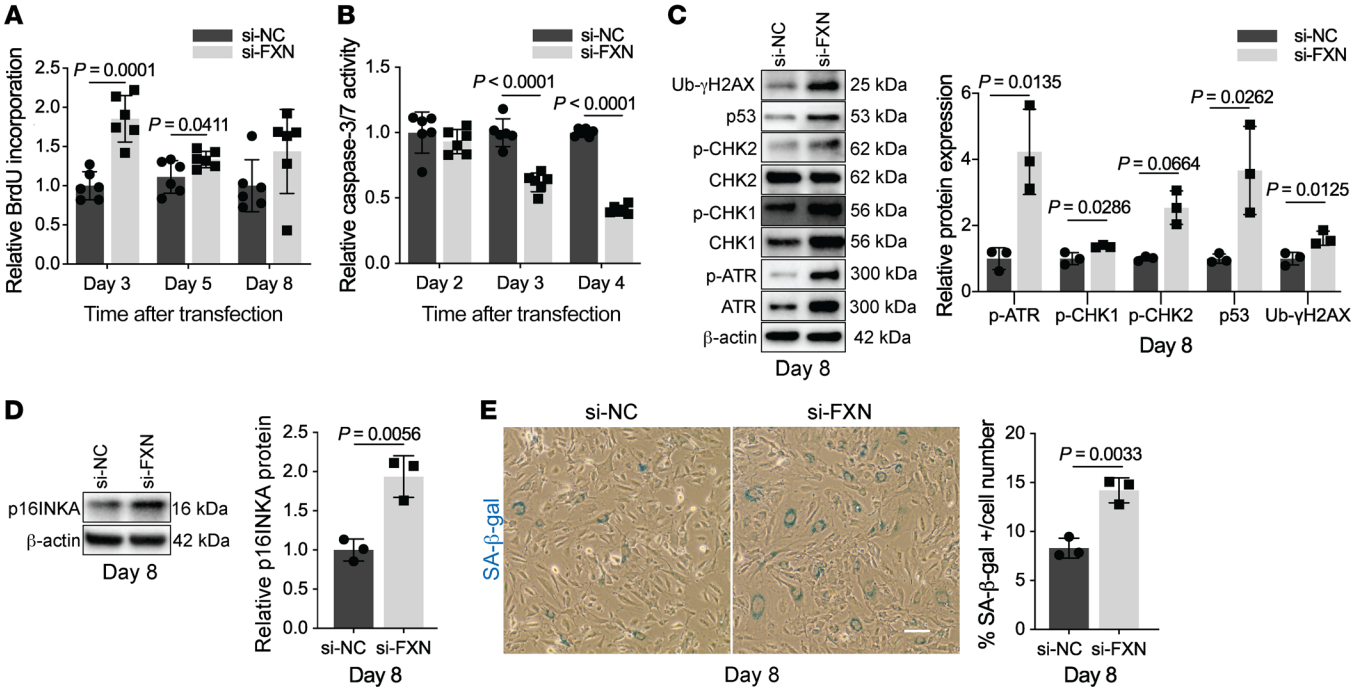

Figure 6. Endothelial progression toward cellular senescence due to chronic FXN deficiency. (**A**) Colorimetric BrdU incorporation in FXN-deficient PAECs compared with negative control at 3, 5, and 8 days after transfection (n = 6/group). (**B**) Chemiluminescent measurement of caspase-3/7 activity in FXN-deficient PAECs compared with controls at 2, 3, and 4 days after transfection (n = 6/group). (**C**–**E**) Experiments reflect PAECs 8 days after transfection with FXN siRNA or negative control (n = 3/group). (**C**) Quantification of DNA damage response markers (p-ATR, p-CHK1, p-CHK2, p53, Ub-γH2AX) by immunoblot. (**D**) Immunoblot of $p16^{INKA}$ protein expression. (**E**) Light microscopic images of SA-β-gal staining (blue). Scale bar: 200 m. Quantification reflects average percentage of SA-β-gal–stained PAECs out of total cell number. Two-tailed Student's t test with error bars that reflect mean ± SD.

intact Fe-S clusters (25, 26). Following transduction with GRX2 versus GCN4 (a homodimer sensor with Fe-S–independent fluorescence), GRX2-specific but not GCN4-specific fluorescence in normoxic (Supplemental Figure 5A) and hypoxic conditions (Supplemental Figure 5B) was reduced in PAECs with siRNA knockdown of FXN (Supplemental Figure 5C).

From there, to determine the predominant pathophenotypes driven by FXN deficiency, an unbiased high-throughput screening by RNA sequencing of differentially expressed genes (498 total genes) was followed by Gene Ontology (GO) enrichment by DAVID in PAECs after FXN knockdown at 2 days after transfection (Supplemental Table 5). Of the top 30 most significant direct GO biological processes (FDR < 0.05, 66 total), a majority were associated with cell cycle (blue), DNA replication (green), and cellular response to DNA damage stimulus (orange) (Figure 4A). Using these GO terms as a guide, a hypergraph, which characterizes differentially expressed genes (nodes) by log fold change and the potential relationships between those nodes via edges (64, 65), highlighted pertinent genes within each selected GO pathway that were significantly upregulated by FXN knockdown (Figure 4B). Given that mitochondrial Fe-S biogenesis influences nuclear Fe-S protein maturation (28, 29), these data support the notion that FXN knockdown could disrupt such Fe-S–dependent genomic stability.

To first assess the functional consequences of these gene changes, replication, a predominant GO pathway (Figure 4), was measured by bromodeoxyuridine (BrdU) incorporation in PAECs. FXN knockdown robustly increased BrdU incorporation (Figure 5A) while overexpression of FXN in combination with its binding partners ISCU1/2 (Supplemental Figure 5, D–G) reversed BrdU incorporation when both endogenous FXN and ISCU1/2 were repressed under chronic hypoxia (Supplemental Figure 6, A and B) or with IL-1β exposure (Supplemental Figure 6, C and D). Despite the increase in nucleotide incorporation, there was no increase in cell number (Figure 5B). Instead, BrdU pulse labeling combined with the fluorescent DNA intercalator 7-AAD revealed an increase of FXN-deficient PAECs in S phase with a corresponding decrease in G0/G1 or G2 (Figure 5C), signifying cell cycle arrest. These data were supported by an increase in the cyclin-dependent kinase inhibitor p21 (Supplemental Figure 6E) associated with DNA damage–dependent cell cycle arrest.

To characterize the potential genomic stress driving S-phase arrest, we found increased protein levels of replication fork components MCM2 and RPA70 (Supplemental Figure 6E), as well as phosphorylated RPA32 in separate male (Figure 5D) and female PAECs donors (Supplemental Figure 6F). Elevation of these markers alongside cell cycle arrest reflected FXN-driven replication stress (15). To assess replication fork dynamics, chloro-deoxyuridine (CldU) and iodo-deoxyuridine (IdU) pulse labeling of DNA fibers in PAECs with FXN inhibition demonstrated a modest increase in CldU nucleotide incorporation (Figure 5E). This FXN-dependent effect was robustly increased with hydroxyurea, a ribonucleotide reductase inhibitor that depletes nucleotide pools to induce fork stalling. This aberrant increase in replication rate correlated with the upregulation of the M2 subunit of ribonu-

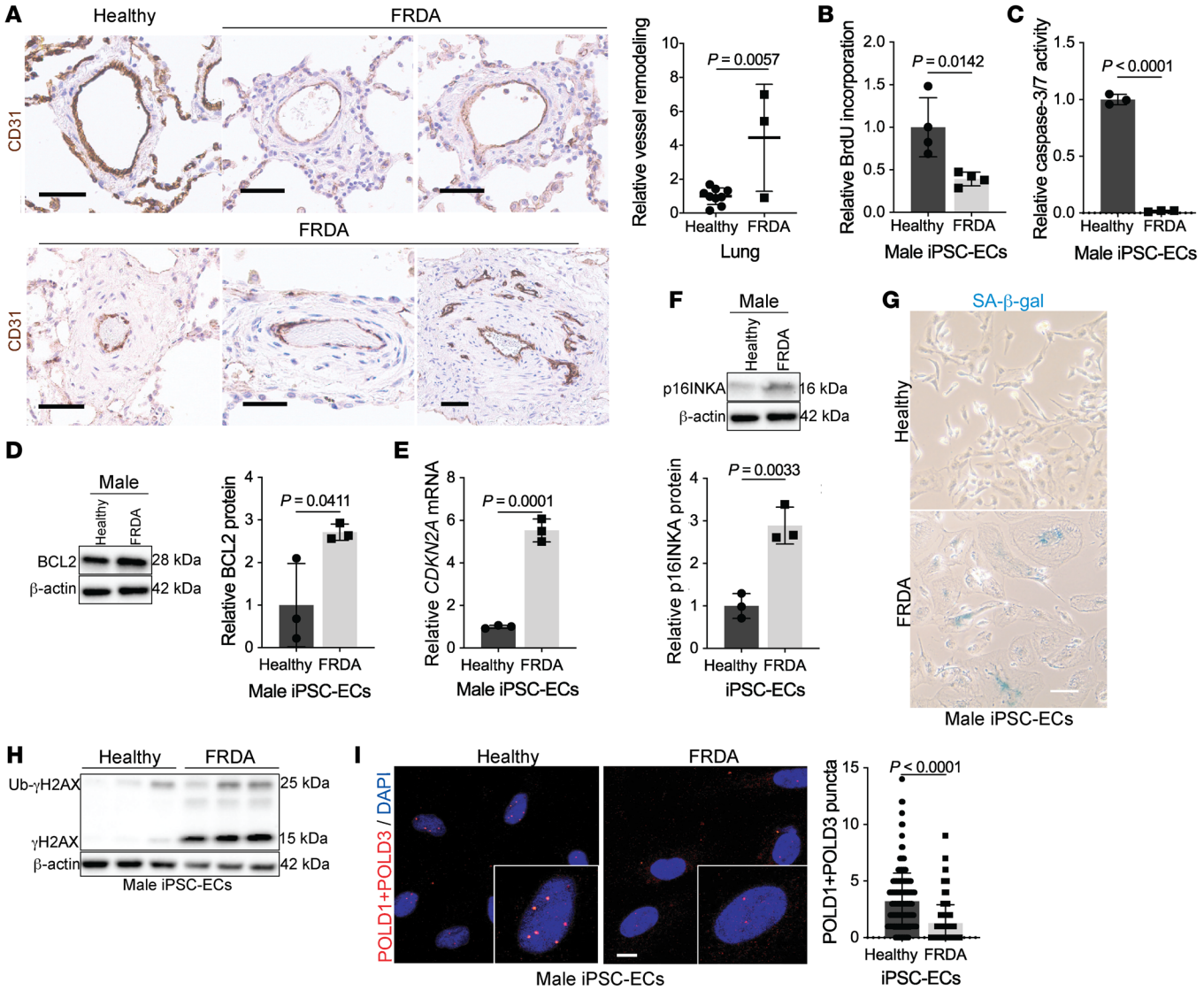

Figure 7. FXN mutations in Friedreich's ataxia are associated with pulmonary vascular disease and endothelial senescence. (**A**) Lungs from age- and sex-matched FRDA (n = 3) versus healthy donors (n = 9) stained with CD31$^+$ (brown) and hematoxylin counterstain (blue). Scale bar: 50 μm. Quantification of relative pulmonary arteriolar wall thickness in FRDA lungs in comparison to controls. Two-tailed Student's t test with error bars that reflect weighted averages ± SD. (**B**–**I**) Phenotypic experiments performed in male age-matched iPSC-ECs from healthy controls versus patients with FRDA. (**B**) Colorimetric BrdU incorporation assay (n = 4/group). (**C**) Chemiluminescent caspase-3/7 activity (n = 3/group). (**D**) Immunoblot quantification of apoptosis resistance BCL2 protein (n = 3/group). (**E** and **F**) Relative *CDKN2A* transcript and p16^{INKA} protein expression in male FRDA iPSC-ECs compared with healthy controls (n = 3/group). (**G**) Representative light microscopic images of β-galactosidase (blue) in male iPSC-ECs. Scale bar: 200 μm. (**H**) Immunoblot of phosphorylated (γH2AX) and ubiquitinated (Ub-γH2AX) forms of H2AX in FRDA patient iPSC-ECs compared with control (n = 3/group). (**I**) Proximity ligation assay followed by confocal microscopy showing quantification of associated POLD1 and POLD3 subunits of DNA Pol δ in FRDA iPSC-ECs compared with healthy controls (n = 190 nuclei/group). Scale bars: 10 μm. The same β-actin blot was used as a control for panels **D** and **K**. Two-tailed Student's t test with error bars that reflect mean ± SD.

cleotide reductase transcript (*RRM2*) (Figure 4B, Supplemental Table 5, and Supplemental Figure 6G), potentially signaling imbalanced nucleotide synthesis by ribonucleotide reductase (66). In response to this replication stress, DDR markers assessed by immunoblot (e.g., phosphorylated ATR, CHK1, and ubiquitinated γH2AX; Figure 5F and Supplemental Figure 6H) and by immunofluorescence staining of 53BP1 foci (Figure 5G) were all upregulated. Conversely, forced expression of FXN in combination with ISCU1/2 cumulatively reduced protein levels of replication stress markers under conditions of hypoxia (Supplemental Figure 6I) or IL-1b (Supplemental Figure 6J), consistent with the acute reversal of replication abnormalities (Supplemental Figure 6, A–D). Notably, FXN knockdown in PASMCs did not result in replication stress or DNA damage response activation (Supplemental Figure 6, K–L), delineating functional differences in endothelial FXN-dependent genotoxic stress. Taken together, these data revealed a specific, reversible mechanism by which acute FXN deficiency drives replication stress, resulting in genomic damage, early activation of the DDR, and endothelial cell cycle arrest.

Sustained DNA damage response results in senescence in FXN-deficient endothelial cells. Because cell cycle arrest can result in apoptosis or senescence (18), we next sought to determine the outcomes

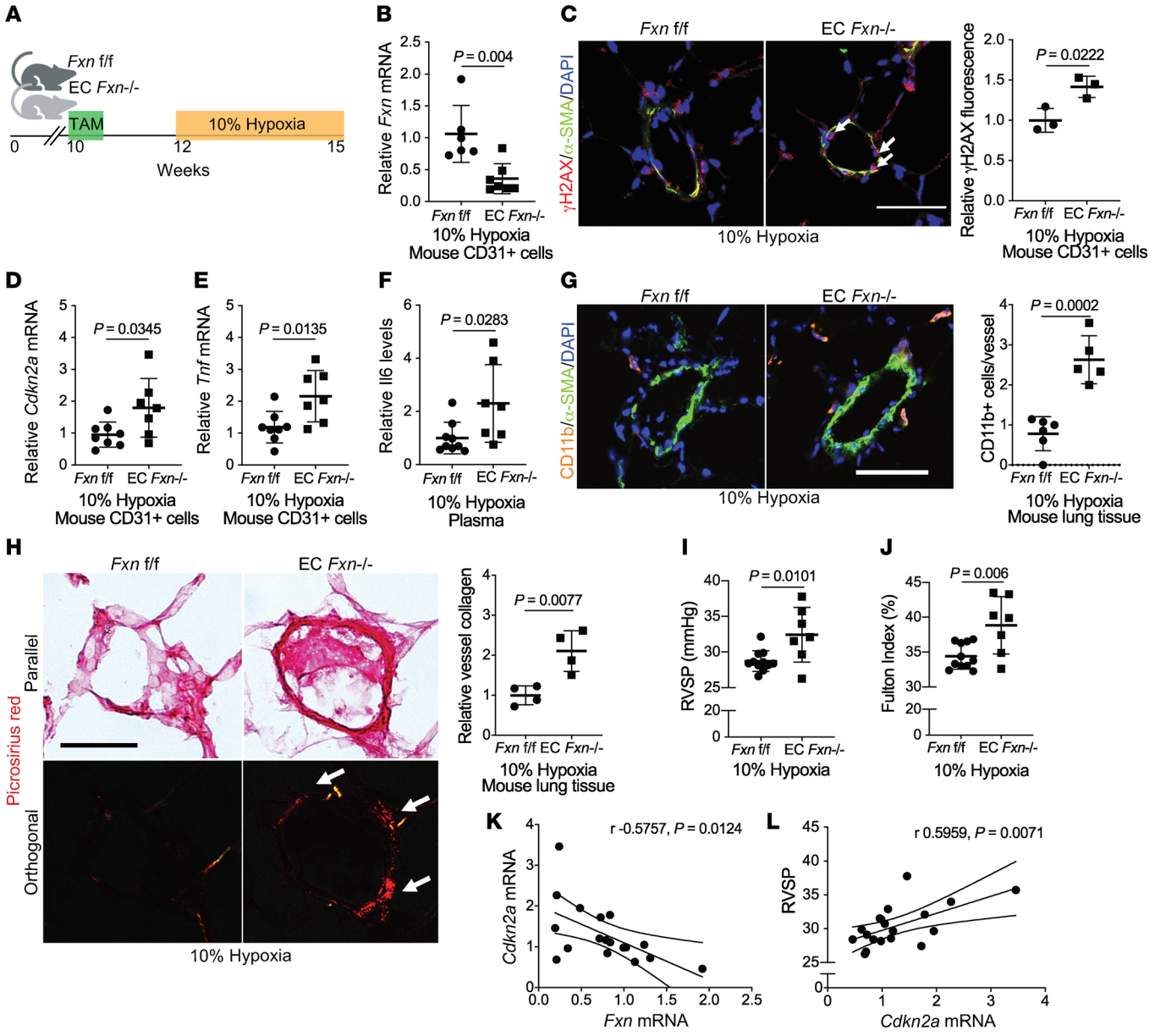

Figure 8. FXN deficiency promotes endothelial senescence and worsens PH in vivo. (**A**) Diagram of conditional endothelial-specific Fxn knockout mouse model. Experiments compare male Fxn *flox/flox* (*Fxn*$^{f/f}$) control mice to mice expressing a tamoxifen-dependent Cdh5(PAC)-ERT2^{+}-Cre recombinase (EC *Fxn*$^{-/-}$) following chronic hypoxia exposure (3 weeks, 10% O_2). (**B**) RT-qPCR of *Fxn* expression in CD31^{+} cells isolated from lungs (n = 6–7/group). (**C**) Confocal microscopic imaging and quantification of endothelial γH2AX (red signal represented by white arrows), α-SMA (green), and DAPI (blue) in lung tissue (n = 3/group). (**D** and **E**) Relative *Cdkn2a* and *Tnf* mRNA by RT-qPCR in CD31^{+} cells isolated from mouse lungs (n = 6–7/group). (**F**) Plasma IL-6 protein expression (n = 9 versus n = 7). (**G**) Measurement of immunofluorescent staining of vessel-associated Cd11b^{+} myeloid cells (orange), α-SMA (green), and DAPI (blue) in lung tissue (n = 5–6/group). (**H**) Picrosirius red staining in parallel versus orthogonal light with quantification of orthogonal signal representative of vessel collagen deposition (n = 4/group). (**I**) RVSP (mmHg) measured by right heart catheterization (n = 11 versus n = 7). (**J**) Fulton index (RV/LV+S, %) (n = 11 versus n = 7). (**K**) Pearson correlation between relative *Fxn* and *Cdkn2a* transcript levels (n = 18). (**L**) Pearson correlation between *Cdkn2a* expression and RVSP (n = 18). Scale bars: 50 μm. Two-tailed Student's t test was performed with error bars that reflect mean ± SD.

of chronic FXN deficiency in the pulmonary endothelium induced by siRNA in PAECs over an extended time course (Supplemental Figure 7, A and B). Interestingly, the initial burst of BrdU incorporation in FXN-deficient PAECs was blunted between days 3 and 8 after transfection (Figure 6A). At the same time, chronic FXN knockdown resulted in increasing apoptosis resistance (starting at 3 days after transfection) in PAECs (Figure 6B). While *RRM2* transcript (Supplemental Figure 7C) and replication stress markers (Supplemental Figure 7D) peaked and were eventually reduced at day 8, FXN-deficient PAECs exhibited chronic and more comprehensive activation of the DDR including ATR, CHK1, CHK2, p53, and γH2AX (Figure 6C). In contrast to other studies in which DNA damage and DDR activation resulted in pulmonary endothelial apoptosis (19, 22), sustained FXN knockdown led to upregulation of the senescence marker p16^{INK4} protein expression (Figure 6D) alongside increased SA-β-gal staining (Figure 6E). Given the irre-

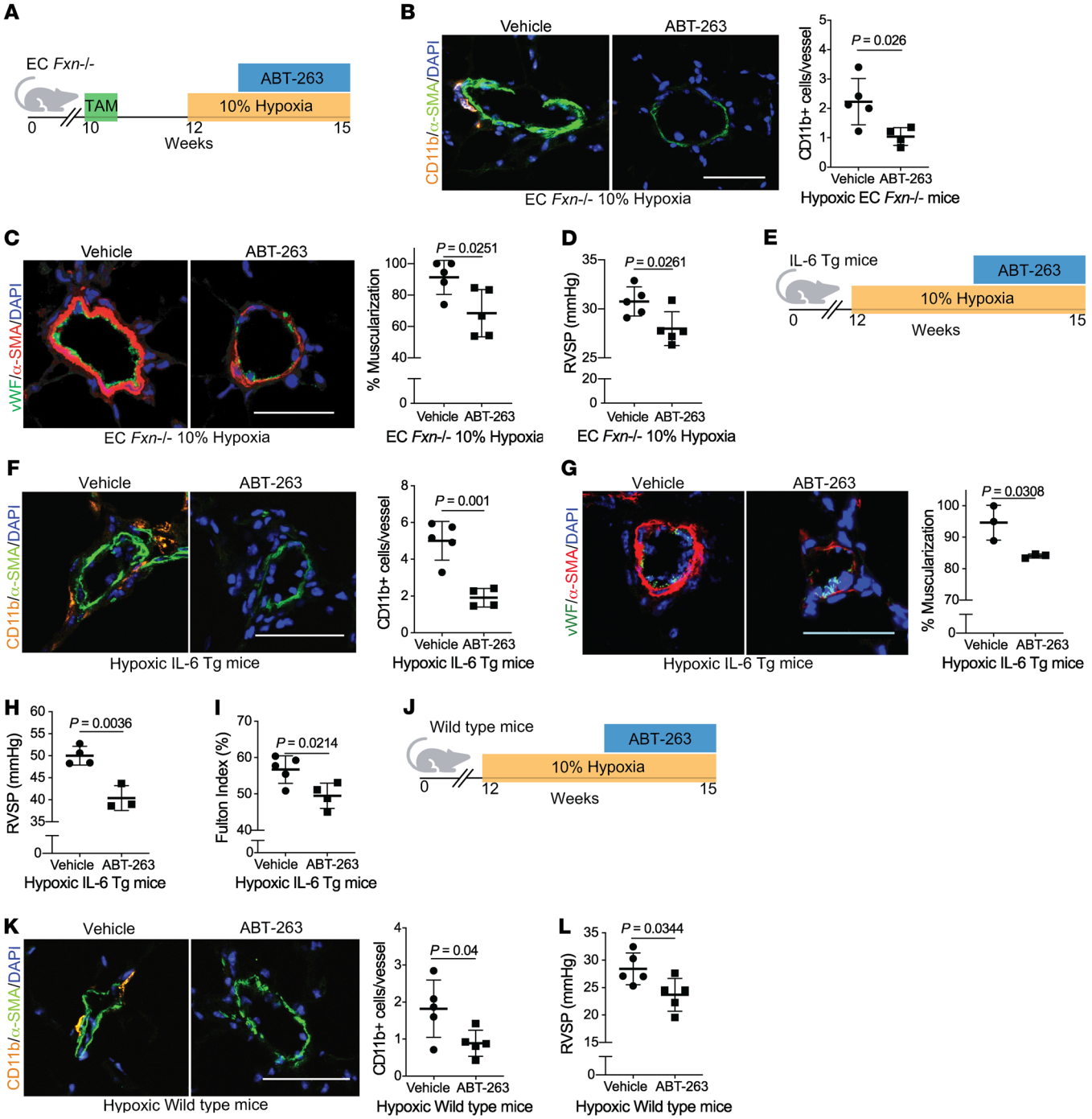

Figure 9. Senolytic therapy prevents FXN-dependent PH development. (**A**) Diagram for senolytic treatment in female and male hypoxic EC *Fxn*$^{-/-}$ mice. ABT-263 (25 mg/kg/day) or vehicle control (n = 5/group) was administered via oral gavage in weeks 2 and 3 of hypoxic exposure (3 weeks, 10% O_2). (**B**) Immunofluorescence staining and assessment of Cd11b$^+$ myeloid cells (orange), α-SMA$^+$ vessel smooth muscle cells (green), and counterstaining of nuclei (blue). (**C**) Representative confocal images and quantified percentage of pulmonary vessel muscularization by immunofluorescence staining of vWF (green) and α-SMA (red). (**D**) RVSP (mmHg). (**E**) Diagram depicting senolytic treatment in female and male IL-6 Tg mice during weeks 2 and 3 of hypoxic exposure. (**F**) Measurement of vessel-associated inflammatory infiltration via Cd11b (orange) (n = 5 versus n = 4). (**G**) Representative images and quantified percentage of vessel muscularization measured by immunofluorescence staining of vWF (green) and α-SMA (red) (n = 3/group). (**H**) RVSP (n = 4 versus n = 3). (**I**) Fulton index (RV/LV+S, %) (n = 5 versus n = 4). (**J**) Diagram of male hypoxic WT mice treated with ABT-263 (n = 5/group). (**K**) Vessel-associated CD11b$^+$ cells. (**L**) RVSP. Two-tailed Student's t test was performed with error bars that reflect mean ± SD. Scale bars: 50 μm.

versible nature of cellular senescence, forced expression of FXN, even in combination with ISCU1/2, did not significantly alter p16^{INK4A} in PAH PMVECs and thus was not able to rescue an already permanent senescent phenotype (Supplemental Figure 7E). Rather, only the senolytic drug ABT-263 (Navitoclax), a BCL2 inhibitor that kills senescent cells (67), was found to abrogate SA-β-gal lev-

els in PAECs with chronic FXN deficiency (Supplemental Figure 7F). In sum, acquired FXN deficiency promotes Fe-S–dependent nuclear dysfunction in primary endothelial cells, displaying a progression of events starting with replication stress and growth arrest and progressing to persistent DDR-dependent senescence.

Genetic FXN deficiency mirrors the genomic dysfunction that drives endothelial senescence. Independent of acquired causes of endothelial FXN reduction, we sought to establish the relevance of endothelial dysfunction to pulmonary vascular remodeling in FRDA. Examining rare lung autopsy samples of 3 individuals with FRDA, histology revealed significant pulmonary arteriolar remodeling (Figure 7A and Supplemental Table 6) in the medial and adventitial layers with indications of inflammatory cell infiltration, strengthening the principle that FRDA and PH are linked. To link causatively genetic FXN deficiency to endothelial dysfunction, we differentiated inducible pluripotent stem cells from patients with FRDA mutations (68) into endothelial cells (iPSC-ECs), as previously described (69). Importantly, iPSC-ECs from patients with FRDA exhibited normal endothelial cell expression markers (Supplemental Figure 8, A and B), function (Supplemental Figure 8C), and markedly reduced FXN levels (Supplemental Figure 8, D and E). Via these genetically FXN-deficient cells and their sex- and age-matched controls, we sought to compare endothelial-specific alterations controlled by FRDA mutations versus acquired deficiencies.

Similar to chronic siRNA FXN knockdown in PAECs, both male and female iPSC-EC lines displayed decreased proliferative (Figure 7B and Supplemental Figure 8F) and apoptotic activity (Figure 7, C and D and Supplemental Figure 8, G and H) and a concomitant increase in cellular senescence markers (Figure 7, E–G and Supplemental Figure 8I). This senescent phenotype was confirmed by elevated inflammatory SASP marker *IL6* (Supplemental Figure 8J) and a reduction in *RRM2* transcript expression (Supplemental Figure 8K). Notably, forced expression of FXN did not substantially reverse senescent markers (Supplemental Figure 8L), consistent with the irreversible nature of senescence (13). To assess whether the DDR response present with FXN siRNA knockdown is mirrored by genetic mutations, immunoblot showed markedly increased ubiquitinated and phosphorylated H2AX in FRDA iPSC-ECs (Figure 7H). Given this FXN-dependent genotoxicity, we aimed to demonstrate that FXN deficiency directly impairs nuclear replication and repair machinery using a proximity ligation assay to assess the Fe-S–dependent association of the DNA polymerase δ catalytic subunit POLD1 with its accessory subunits, in this case, POLD3 (70). Confocal imaging showed iPSC-ECs with FRDA mutations exhibited decreased nuclear signal, denoting a FXN-driven reduction in the intact form of this high-fidelity polymerase (Figure 7I). Therefore, these findings delineate an FXN-driven mechanism in which persistent attenuation of Fe-S–containing nuclear machinery may compromise DNA replication and repair, contributing to endothelial senescence.

Genetic and pharmacologic endothelial FXN deficiency in mice promotes senescence and consequent PH. To investigate the specific effects of FXN deficiency in the pulmonary endothelium in vivo, both genetic and pharmacologic Fxn knockdown mouse models were investigated. First, tamoxifen-dependent endothelial (EC) *Fxn*$^{-/-}$ mice (Cdh5(PAC)–Cre-ERT2+ mice [71] crossed with Fxn *flox/flox* mice; ref. 72) were exposed to normoxia vs. chronic hypoxia to induce PH (Figure 8A). CD31^{+} pulmonary endothelial cells from EC *Fxn*$^{-/-}$ mice exhibited appropriate cell-type specific knockout (Supplemental Figure 9A) and decreased *Fxn* transcript (Figure 8B). Consistent with the efficiency of this endothelial-specific Cre recombinase (71), such knockout was not fully penetrant in all endothelial cells and thus served as an optimal model for heterogeneity of FXN reduction seen in human PAH disease (Figure 2, D and E). To rule out any off-target effects relevant to the left ventricle or systemic hypertension, echocardiographic imaging prior to hemodynamic measurements demonstrated no gross alterations in left ventricular function (Supplemental Figure 9, B and D). Additionally, no alterations in mean arterial pressure (Supplemental Figure 9E) and heart rate (Supplemental Figure 9F) were observed. Consistent with our findings of FXN-driven genotoxicity in vitro (Figures 6 and 7), confocal imaging revealed that EC *Fxn*$^{-/-}$ mice displayed increased DDR marker γH2AX in the pulmonary endothelium (Figure 8C). At the same time, RT-qPCR analysis of isolated pulmonary CD31^{+} endothelial cells from FXN-deficient mice displayed an increase in *Cdkn2a* and the inflammatory SASP markers *Tnf* and Il-6, signifying stable growth arrest and elevated SASP, respectively (Figure 8, D–F). Guided by the presence of such SASP-driven inflammatory signaling, elevated accumulation of CD11b^{+} interstitial myeloid cells was observed in the pulmonary vasculature (Figure 8G), mirroring the inflammatory remodeling in FRDA lungs (Figure 7A). While medial thickening was not significantly increased (Supplemental Figure 9G), lungs from hypoxic EC *Fxn*$^{-/-}$ mice exhibited an increase in vascular collagen matrix remodeling (Figure 8H), mirroring the adventitial remodeling in FRDA lungs (Figure 7A). Correspondingly, right heart catheterization revealed hemodynamic manifestations of worsened PH, including increased right ventricular systolic pressure (RVSP, a surrogate for the clinical measurement of mean pulmonary arterial pressure [mPAP]; Figure 8I), and increased Fulton index (a measurement of RV hypertrophy that indirectly reflects increased pulmonary vascular resistance; Figure 8J) in endothelial Fxn-deficient mice. Importantly, consistent with single-cell RNA sequencing data from human PAH lung (Figure 2F), an inverse correlation between Fxn expression and *Cdkn2a* was observed (Figure 8K). This was accompanied by a positive correlation between *Cdkn2a* and RVSP (Figure 8L). Thus, these results emphasize the pathogenic role of a FXN-deficient senescent subpopulation in the pulmonary endothelium that promote vascular inflammation, remodeling, and PH.

In contrast, normoxic EC *Fxn*$^{-/-}$ mice did not display hemodynamic manifestations of PH (Supplemental Figure 9, H and I), suggestive that a second hit may bolster a more robust vascular pathophenotype. Furthermore, chronically hypoxic, tamoxifen-dependent smooth muscle–specific (73) *Fxn*$^{-/-}$ mice (Supplemental Figure 9J) did not exhibit a difference in RVSP (Supplemental Figure 9K) or Fulton index (Supplemental Figure 9L) compared with *Fxn*$^{+/+}$ controls, correlating with the lack of genotoxic stress seen with FXN knockdown in PASMCs (Supplemental Figure 6, K and L) and reinforcing the importance of endothelial FXN deficiency in PH.

Moving to a pharmacologic model of endothelial FXN deficiency, polymeric nanoparticle 7C1, composed of low-molecular-weight polyamines and lipids encapsulating Fxn siRNA

oligonucleotides or negative control, were delivered to the endothelium via tail-vein injection every 5 days in WT C57BL/6 mice briefly before and throughout chronic hypoxia exposure (Supplemental Figure 10A and refs. 25, 26, 74). In mice receiving inhibitory RNA against Fxn, *Fxn* was downregulated in $CD31^+$ cells as assessed by RT-qPCR (Supplemental Figure 10B). Consistent with FXN-dependent genotoxic stress, 7C1:siFXN administration increased vessel γH2AX levels (Supplemental Figure 10C). Unlike hypoxic EC $Fxn^{-/-}$ mice, hypoxic 7C1:siFXN mice exhibited increased medial thickening as measured by α-SMA immunofluorescence staining (Supplemental Figure 10D) and hemodynamics consistent with PH development (Supplemental Figure 10, E and F). These Fxn-deficient mice did not demonstrate changes in mean arterial pressure (Supplemental Figure 10G), or heart rate (Supplemental Figure 10H). Notably, even in normoxia, 7C1-delivered FXN siRNA (Supplemental Figure 10I) elicited a modest but significant increase of RVSP and Fulton index (Supplemental Figure 10, J and K), again indicating that FXN deficiency predisposes the endothelium to a PH-prone phenotype that could then be augmented by additional injury or stress. Therefore, as displayed through both genetic and pharmacologic models, FXN deficiency drives endothelial senescence with downstream vascular inflammation and remodeling, thereby promoting PH in vivo.

Pharmacologic removal of senescent cells prevents PH pathogenesis in FXN-deficient models. Finally, we sought to explore the contribution of FXN-dependent endothelial senescence to the development of multiple PH subtypes in vivo. To do so, we wanted to determine if pharmacologic clearance of senescent cells by the BCL2 inhibitor ABT-263 (67) could reverse FXN-dependent disease. First, EC $Fxn^{-/-}$ mice were exposed to hypoxia and serial gavages of vehicle versus ABT-263 (Figure 9A). Neither hepatic nor renal toxicity was evident with such dosing (Supplemental Figure 11, A–D). Despite persistent pulmonary endothelial Fxn deficiency (Supplemental Figure 11E), removal of senescent cells led to diminished vascular disease, as measured by CD11b accumulation (Figure 9B) and muscularization (Figure 9C). Correspondingly, ABT-263 treatment reduced RVSP in Fxn-deficient mice (Figure 9D).

To determine whether senolysis could prevent PH development across different mouse models and disease subtypes that also exhibit FXN deficiency, hypoxic IL-6 Tg mice (modeling Group 1 PAH) were also treated with ABT-263 compared with vehicle (Figure 9E). This model was chosen for study due to its direct links to the FXN-senescence axis. Not only was FXN downregulated by IL-6 (Supplemental Figure 1C and Supplemental Figure 2C), but also IL-6 plays a central role in senescence as both an paracrine SASP factor as well as an autocrine effector that reinforces senescence in the source tissue (75). Again, upstream Fxn expression remained depressed (Supplemental Figure 11F), and there was no evidence of liver or kidney damage (Supplemental Figure 11, G–J). Yet, senolytic administration reduced SASP-dependent interstitial immune cell elevation in the vasculature (Figure 9F), vessel remodeling (Figure 9G), and consequent hemodynamic manifestation of PAH (Figure 9, H and I), thus proving the crucial role of cellular senescence in halting the pathogenic cycle connecting FXN deficiency to PAH.

Lastly, hypoxic WT mice (modeling Group 3 PH) — which also exhibit pulmonary endothelial Fxn deficiency (Supplemental Figure 11, K and L) — treated with a senolytic (Figure 9J and Supplemental Figure 11, M–Q) exhibited reduced vessel-associated inflammation and PH disease burden (Figure 9, K and L). These data support the notion that endothelial-specific FXN deficiency drives senescence, remodeling, and PH, and that this Fe-S–driven mechanism is necessary to promote disease in several preclinical rodent models representing WSPH Groups 1 and 3.

Discussion

Via discovery platforms spanning single-cell RNA sequencing in PAH tissues to genetically engineered mice and rare FRDA patient lungs, our results define endothelial FXN deficiency as a driver of senescence and thus multiple PH subtypes (Graphical Abstract). Coupled with our advancing understanding of endothelial senescence in a variety of vascular diseases (8) and in PAH-associated congenital heart disease (9), these findings address a key knowledge gap regarding the regulation of this pivotal vascular process, with data identifying persons at genetic and acquired risk for PH. At the molecular level, while DNA damage (19–23) has been associated with PH, these data identified FXN-dependent Fe-S biology as a master regulator of genotoxic stress and downstream endothelial dysfunction in this disease. At a cellular level, our work provides a molecular explanation underlying the development of heterogeneous endothelial pathophenotypes in PH — where FXN deficiency generates a senescent subpopulation of endothelial cells which then promotes inflammation-associated vascular remodeling. At a disease level, these results demonstrate that FXN-dependent endothelial senescence is central in promoting multiple PH subtypes, across WSPH Groups 1, 2, and 3. In FRDA and Group 2 PH, our work implicates FXN-dependent endothelial pathogenicity and challenges the current paradigm of cardiomyocyte dysfunction and consequent hemodynamic stress as the sole causes of PH. Our endeavors also strengthen the notion for therapeutic development of senolytic drugs that reverse the effects of Fe-S deficiency, applicable across multiple PH subtypes, several of which have no approved therapies.

Our data highlight how triggers of PH, such as chronic hypoxia and inflammation, converge upon HIF-α–mediated CTCF epigenetic modification of *FXN* transcription in endothelial cells (Figure 3). Given that prior studies identified a HIF-α–dependent increase of FXN in nonvascular cells (39, 40), the reasons for divergent gene regulation in the pulmonary endothelium are not fully understood. There may be cell-type specificity of the chromatin structure and its modulators (i.e., CTCF) in exerting control of FXN. Importantly, identification of this HIF-α/CTCF axis expands upon the relevance of acquired FXN deficiency outside of FRDA mutations. FXN also joins a growing number of Fe-S assembly genes dynamically repressed by HIF-α signaling in the endothelium (24–26). While certain FXN-dependent phenotypes share similarities with those resulting from deficiencies of other HIF-α–dependent Fe-S biogenesis genes (*ISCU* and *BOLA3*; refs. 24–26), each Fe-S assembly protein exerts unique and predominant effects on endothelial phenotypes (proliferation promoted by BOLA3 deficiency [26], apoptosis by ISCU deficiency [24], senescence by FXN deficiency). It is possible that these HIF-α–driven deficiencies

and their specific cell fates cumulatively contribute to the shifting endothelial pathophenotypes throughout PH progression and across WSPH classifications. However, the contributions of this dynamic network of Fe-S biogenesis genes are only just emerging.

In addition, our data provide insight into the potential interaction between hypoxia and genetic FXN deficiency. Recent findings reported that exposing FXN-depleted models to anaerobic conditions may rescue Fe-S biogenesis, reverse the FRDA-specific ataxia phenotype, and improve viability — all of which suggest hypoxic exposure may be a useful therapy for patients with FRDA (76). In contrast, our data demonstrated that chronic low oxygen tension reduced Fe-S biogenesis gene expression (*FXN*, *ISCU*, and *BOLA3*) in pulmonary vascular cells, particularly in endothelial cells (24–26). These results are supported by prior findings in other hypoxic cell types (41, 77). More specifically, in our work, hypoxic PAECs with FXN knockdown showed reduced Fe-S cluster formation compared with control (Supplemental Figure 5B), indicating that anaerobic conditions do not rescue endothelial Fe-S biogenesis. Because several PH outcomes, including hemodynamic assessment (Figure 8 and Supplemental Figure 10), worsened with a 2-hit model of endothelial FXN knockdown and chronic hypoxia, our data caution against the systemic use of hypoxia treatment in FRDA, which would not account for differences in cell-specific responses to hypoxia and instead could accelerate a patient's predisposition to PH.

Next, our findings illustrate Fe-S–dependent perturbations in genomic integrity with FXN deficiency. Acutely, the increased FXN-dependent replication rate (Figure 5A) has recently been identified as a lesser-known form of replication stress that promotes DDR and ultimately genomic instability (78). Given increased *RRM2* expression (Supplemental Figure 6G), upregulation in replication fork elongation may be driven at least in part by altered ribonucleotide reductase (RNR) activity and a consequent imbalance in the nucleotide pools, both of which have been shown to impact DNA integrity (79). Interestingly, RNR contains an essential di-ferric tyrosyl radical cofactor donated by cytoplasmic Fe-S machinery (66), and its activity is preferentially preserved in the early stages of iron deficiency in yeast (80). This same acute sequestration of iron cofactors and conserved function may be characteristic of other Fe-S–containing DNA replication and repair machinery in conditions of acute FXN deficiency. In our work, *RRM2* expression (Supplemental Figure 6G and Supplemental Figure 7C) also follows the simultaneous arc of nucleotide incorporation (Figure 5A and Figure 6A) and replication fork markers (Supplemental Figure 6E and Supplemental Figure 7D) from acute replication stress to eventual senescence. Similar to *RRM2*-deficient cancer cells exhibiting long-term senescence-associated growth arrest (81), our findings may reflect diminished RNR activity that leads to replication collapse and stable growth arrest. Separately, we showed that genetic FXN deficiency disrupts Fe-S–dependent DNA Pol δ structure and function (Figure 7I), alongside persistent elevation of DDR markers (Figure 7H). Given that DNA polymerases, among other Fe-S–containing proteins, are critical for several DNA repair pathways (28, 70), FXN-specific attenuation of Fe-S–dependent nuclear protein function may propagate endothelial genomic instability and thus DDR and senescence.

While our findings begin to characterize genome-specific perturbations driven by FXN deficiency, the exact pattern of disruption in Fe-S–reliant nuclear machinery that converges on irreversible growth arrest merits further interrogation. More broadly, given the known mitochondrial and metabolic activities of FXN (27) and other Fe-S biogenesis genes (24–26), metabolic oxidative stress could also contribute to alterations in genomic integrity and cell cycle progression (82). In fact, DNA damage has been observed in FRDA patient tissues previously, presumed to result from incompletely defined oxidative processes (50, 51). Moreover, disruption of mitochondrial function has been shown to contribute to cellular senescence (mitochondria dysfunction–associated senescence) (83). The exact contribution of FXN-dependent metabolic disruption to progression toward endothelial senescence awaits further study. It is also possible that a combination of these pathogenic processes — for example, oxidative stress and failure of Fe-S–dependent replication — represents a double-hit to genomic integrity. It is not known which of these FXN-dependent processes is more effective in initiating replication stress, genomic damage, and reversible versus irreversible growth arrest. These answers may help prioritize early treatment intervention, given that there may be a critical window for phenotypic rescue (Supplemental Figure 6, A–D, I, and J) prior to permanent endothelial senescence (Supplemental Figure 7E).

Apart from defining how FXN-dependent genotoxic stress converges on irreversible growth arrest, our data depict a subpopulation of FXN-deficient senescent endothelial cells that direct panvascular remodeling in PH. In contrast to a widely touted model of temporal progression of dominant endothelial pathophenotypes in PH (7), our findings underscore a different paradigm whereby senescent endothelial cells stochastically depend on FXN deficiency but do not need to predominate in number to exert a pathogenic influence. Rather, we found that senescent endothelial cells promote local inflammation and pulmonary vascular remodeling through the release of SASP mediators. Specifically, IL-6, a cytokine already identified as a prognostic indicator of severe PH (58, 84–86), represents at least a proinflammatory mediator produced by FXN-deficient senescent endothelial cells (Figure 8, E and F and Supplemental Figure 8J). Given that the SASP profiles depend on cell type, inciting factors of senescence, or degree of senescence (13), the full complement of FXN-dependent markers requires further study. Via this autocrine signaling, senescent endothelial cells inherently coexist with other proliferative cells (Figure 2D), offering a molecular description for a heterogenous endothelium in PH.

Despite observed FXN reduction in smooth muscle cells across multiple PH models (Supplemental Figures 1 and 2), FXN deficiency in smooth muscle cells did not result in the same genotoxic mechanism (Supplemental Figure 6, K and L) and subsequent PH development (Supplemental Figure 9, J–L). Taking cues from patients with FRDA with ubiquitous deficiency yet cell-specific symptomatic pathology (e.g., dorsal root ganglion and corresponding ataxia), there may be differences in relative basal FXN expression, sensitivity to FXN downregulation, or potential compensatory mechanisms that explain the pathological importance of endothelial compared with smooth muscle FXN and Fe-S cluster deficiency.

Our observations also offer a mechanistic explanation for a predisposition to precapillary PH across multiple WSPH subtypes. A role for FXN in Groups 1 and 3 PH is not surprising, given our prior findings of ISCU1/2- and BOLA3-dependent Fe-S pathobiology in these disease subtypes (24–26). Yet, while HCM drives mortality in patients with FRDA (44) and patients with HCM generally suffer from precapillary PH (46, 47), our data suggest a genetic predisposition to endothelial dysfunction that drives pulmonary vascular disease (Figure 7A and ref. 45). In this way, our work offers a paradigm whereby a vascular endothelium, already primed to remodel, promotes PH alongside cardiomyocyte dysfunction and left atrial overload. Given that the trinucleotide repeat mutations in FRDA result in endothelial FXN deficiency in multiple vascular beds, coronary or cardiac microvascular endothelial senescence may also act as a driver of worsened ischemic cardiomyopathy, thus compounding the stress on the pulmonary vasculature. Future studies are warranted to elucidate the individual or additive effects of endothelial FXN deficiency in the setting of FRDA-specific HCM. In addition, given that animal models of Group 2 PH due to HFpEF showed decreased Fxn and increased *Cdkn2a* (Figure 1, E and F), it is possible that this endothelial mechanism contributes to inherent pulmonary vascular dysfunction in Group 2 PH in general, potentially reinforcing the currently unproven notion that Group 1–like primary vascular pathophenotypes contribute to Group 2 PH (i.e., Cpc-PH; ref. 87) and are not solely due to cardiomyocyte dysfunction, leading to increased left heart afterload (47, 88). Moreover, since the age of prevalent patients with PH is increasing worldwide and older patients with PH are more commonly afflicted by HFpEF (89), FXN-dependent endothelial senescence, an age-associated phenotype (90, 91), could also serve as a key molecular driver for PH in the elderly. These data may ultimately provide a foundation for the identification and management of a cohort of FXN-deficient patients at risk for PH who might benefit from preexisting or emerging PH therapies (2).

Finally, our FXN-driven model of endothelial senescence may provide Fe-S–dependent targets for diagnostic and therapeutic intervention. In particular, endothelial senescence is an emerging characteristic of vascular diseases and may be improved with targeted pharmacologic intervention (8). In addition to prior data on the use of senolytic therapy in experimentally induced PH due to cardiac shunts (9), our data demonstrate the therapeutic efficacy of senolysis to prevent FXN-driven vessel-associated inflammatory remodeling and hemodynamic instability across several PH models (Figure 9). Additional studies may help determine whether senolytics (92) may be beneficial in patients with FRDA and with PH generally. If so, given the irreversible nature of senescence, appropriate therapeutic timing of these drugs will be crucial during PH development, as will determination of their efficacy in young versus old patients.

In total, this work offers a unifying Fe-S–dependent mechanism explaining the dynamic progression of endothelial phenotypes across multiple PH etiologies. We delineate an endothelial-specific predisposition to PH for FRDA and potentially other forms of Group 2 PH. More broadly, our findings connect the regulatory actions of FXN across Fe-S biology, genomic integrity, and senescence, and presents targets for more effective diagnostics and therapeutics in this deadly disease.

Methods

High-throughput RNA sequencing. Following broad range RNA Qubit quality control and long RNA sequencing (paired-end read 75 cycles, 40–50M reads/sample), transcript quantification was performed using Salmon and differential expression using DESEQ (93, 94). See Supplemental Material for additional detail. The complete data set is available in the GEO repository via the accession number GSE171692.

Study approval. All animal experiments were approved by the University of Pittsburgh (DLAR) and the Harvard Center for Comparative Medicine. Informed consent was obtained for patient right heart catheterization and tissue sampling for research use. All experimental procedures involving the use of human tissue and plasma, and the study of invasive and noninvasive hemodynamics were approved by the IRBs at the University of Pittsburgh and the Mayo Clinic. Ethical approval for this study and informed consent conformed to the standards of the Declaration of Helsinki.

Statistics. The number of animals in each group was calculated to measure at least 20% difference between the means of experimental and control groups with a power of 80% and standard deviation of 10%. The number of unique patient samples for this study was determined primarily by clinical availability. All in vitro data represent at least 3 independent experiments and are presented as mean ± SD. Normality of data distribution of groups with n greater than 10 was determined by Shapiro-Wilk testing. Paired samples were compared by a 2-tailed Student's t test for normally distributed data, while Mann-Whitney U nonparametric testing was used for nonnormally distributed data. For comparisons among groups, 1-way or 2-way ANOVA with post hoc Tukey's analysis to adjust for multiple comparisons were performed. A P value less than 0.05 was considered significant. Additional methods and complete unedited blots are available in the supplemental material.

Author contributions

MKC, JZ, AUG, and SYC conceived and designed the experiments. MKC, JZ, YYT, YT, DP, TB, QY, VN, CSCW provided the experimental infrastructure and performed the experiments. AH, GS, and SK performed in silico analyses of long RNA sequencing. RL provided data. AH and SYC performed analyses of single-cell RNA sequencing. YCL and MTG provided OCT-embedded and flash-frozen lung tissue from ZSF1 rats. TS performed the rodent echocardiography. AUF, MMR, AMMW, YAA, JS, M Rojas, EAG, and DG performed the work to obtain human tissue samples. OFK, DGA, and JED helped prepare and perform the 7C1 nanoparticle murine experiments. MG differentiated FRDA mutant iPS cells into endothelial cells, and MG and M Rabinovitch provided iPS-derived healthy control endothelial cells. MKC and SYC wrote the manuscript. All authors participated in interpreting the results and revising the manuscript.

Acknowledgments

This work was supported by NIH grants F30 HL139017 (to MKC); R01 HL124021, HL122596, HL138437, and UH2/UH3 TR002073 (to SYC); American Heart Association Established Investigator Award 18EIA33900027 (to SYC); NIH K99 HL135258 (to MG); NIH S10OD023684 (Instrument Grant); NIH R01 HL113178 and R01 HL130261 (to EAG); the Koch Institute Support (core) Grant P30-CA14051 from the National Cancer Institute; the United States

Army Medical Research and Materiel Command's Armed Forces Institute of Regenerative Medicine grant W81XWH-08-2-0034 (to OFK); and the French National Research Agency grant ANR-18-CE14-0025 (to TB). We thank J. Silberg (Rice University) for the GRX2 and GCN4 sensor plasmids. We thank W. Horne and the Health Sciences Sequencing Core (UPMC Children's Hospital of Pittsburgh) for performing RNA sequencing. We thank the University of Pittsburgh Center for Biologic Imaging and the Mayo Clinic Cancer Center Pathology Research Core for technical help and use of their facilities and resources. We thank B. Van Houten for critical advice; R.M. Payne and H. Puccio for providing FXN *flox/flox* mice; R. Adams for providing Cdh5(PAC)-CreERT2 mice; and Y. Lu and S. Annis for technical support. We acknowledge the Center for Organ Recovery & Education, the organ donors, and their families for the human lung tissue samples used in this study.

Address correspondence to: Stephen Y. Chan, Center for Pulmonary Vascular Biology and Medicine, Pittsburgh Heart, Lung, and Blood Vascular Medicine Institute, Division of Cardiology, Department of Medicine, University of Pittsburgh Medical Center, 200 Lothrop Street, BST E1240, Pittsburgh, Pennsylvania 15261, USA. Phone: 412.383.6990; Email: chansy@pitt.edu.

1. Simonneau G, et al. Haemodynamic definitions and updated clinical classification of pulmonary hypertension. *Eur Respir J*. 2019;53(1):1801913.
2. Lai YC, et al. Pulmonary arterial hypertension: the clinical syndrome. *Circ Res*. 2014;115(1):115–130.
3. Prince MJ, et al. The burden of disease in older people and implications for health policy and practice. *Lancet*. 2015;385(9967):549–562.
4. Guazzi M. Pulmonary hypertension in heart failure preserved ejection fraction: prevalence, pathophysiology, and clinical perspectives. *Circ Heart Fail*. 2014;7(2):367–377.
5. Gopal DM, et al. Impaired right ventricular hemodynamics indicate preclinical pulmonary hypertension in patients with metabolic syndrome. *J Am Heart Assoc*. 2015;4(3):e001597.
6. Nathan SD, et al. Pulmonary hypertension in chronic lung disease and hypoxia. *Eur Respir J*. 2019;53(1):1801914.
7. Sakao S, et al. Endothelial cells and pulmonary arterial hypertension: apoptosis, proliferation, interaction and transdifferentiation. *Respir Res*. 2009;10(1):95.
8. Childs BG, et al. Senescent cells: a therapeutic target for cardiovascular disease. *J Clin Invest*. 2018;128(4):1217–1228.
9. van der Feen DE, et al. Cellular senescence impairs the reversibility of pulmonary arterial hypertension. *Sci Transl Med*. 2020;12(554):eaaw4974.
10. Beaulieu D, et al. Phospholipase A2-receptor 1 promotes lung-cell senescence and emphysema in obstructive lung disease. *Eur Respir J*. 2021;2000752.
11. Gulati S, Thannickal VJ. The aging lung and idiopathic pulmonary fibrosis. *Am J Med Sci*. 2019;357(5):384–389.
12. Campisi J, d'Adda di Fagagna F. Cellular senescence: when bad things happen to good cells. *Nat Rev Mol Cell Biol*. 2007;8(9):729–740.
13. Herranz N, Gil J. Mechanisms and functions of cellular senescence. *J Clin Invest*. 2018;128(4):1238–1246.
14. McHugh D, Gil J. Senescence and aging: causes, consequences, and therapeutic avenues. *J Cell Biol*. 2018;217(1):65–77.
15. Zeman MK, Cimprich KA. Causes and consequences of replication stress. *Nat Cell Biol*. 2014;16(1):2–9.
16. Jackson SP, Bartek J. The DNA-damage response in human biology and disease. *Nature*. 2009;461(7267):1071–1078.
17. Roos WP, et al. DNA damage and the balance between survival and death in cancer biology. *Nat Rev Cancer*. 2016;16(1):20–33.
18. Childs BG, et al. Senescence and apoptosis: dueling or complementary cell fates? *EMBO Rep*. 2014;15(11):1139–1153.
19. de Jesus Perez VA, et al. Whole-exome sequencing reveals TopBP1 as a novel gene in idiopathic pulmonary arterial hypertension. *Am J Respir Crit Care Med*. 2014;189(10):1260–1272.
20. Meloche J, et al. Role for DNA damage signaling in pulmonary arterial hypertension. *Circulation*. 2014;129(7):786–797.
21. Federici C, et al. Increased mutagen sensitivity and dna damage in pulmonary arterial hypertension. *Am J Respir Crit Care Med*. 2015;192(2):219–228.
22. Li CG, et al. PPARγ Interaction with UBR5/ATMIN promotes DNA repair to maintain endothelial homeostasis. *Cell Rep*. 2019;26(5):1333–1343.
23. Bourgeois A, et al. Inhibition of CHK1 (checkpoint kinase 1) elicits therapeutic effects in pulmonary arterial hypertension. *Arterioscler Thromb Vasc Biol*. 2019; 39(8):1667–1681.
24. Chan SY, et al. MicroRNA-210 controls mitochondrial metabolism during hypoxia by repressing the iron-sulfur cluster assembly proteins ISCU1/2. *Cell Metab*. 2009;10(4):273–284.
25. White K, et al. Genetic and hypoxic alterations of the microRNA-210-ISCU1/2 axis promote iron-sulfur deficiency and pulmonary hypertension. *EMBO Mol Med*. 2015;7(6):695–713.
26. Yu Q, et al. BOLA (BolA Family Member 3) deficiency controls endothelial metabolism and glycine homeostasis in pulmonary hypertension. *Circulation*. 2019;139(19):2238–2255.
27. Rouault TA, Maio N. Biogenesis and functions of mammalian iron-sulfur proteins in the regulation of iron homeostasis and pivotal metabolic pathways. *J Biol Chem*. 2017;292(31):12744–12753.
28. Fuss JO, et al. Emerging critical roles of Fe-S clusters in DNA replication and repair. *Biochim Biophys Acta*. 2015;1853(6):1253–1271.
29. Paul VD, Lill R. Biogenesis of cytosolic and nuclear iron-sulfur proteins and their role in genome stability. *Biochim Biophys Acta*. 2015;1853(6):1528–1539.
30. Lill R. Function and biogenesis of iron-sulphur proteins. *Nature*. 2009;460(7257):831–838.
31. Olsson A, et al. Myopathy with lactic acidosis is linked to chromosome 12q23.3-24.11 and caused by an intron mutation in the ISCU gene resulting in a splicing defect. *Hum Mol Genet*. 2008;17(11):1666–1672.
32. Ahting U, et al. Clinical, biochemical, and genetic spectrum of seven patients with NFU1 deficiency. *Front Genet*. 2015;6:123.
33. Navarro-Sastre A, et al. A fatal mitochondrial disease is associated with defective NFU1 function in the maturation of a subset of mitochondrial Fe-S proteins. *Am J Hum Genet*. 2011;89(5):656–667.
34. Niihori M, et al. Rats with a human mutation of NFU1 develop pulmonary hypertension. *Am J Respir Cell Mol Biol*. 2020;62(2):231–242.
35. Yu AY, et al. Impaired physiological responses to chronic hypoxia in mice partially deficient for hypoxia-inducible factor 1alpha. *J Clin Invest*. 1999;103(5):691–696.
36. Brusselmans K, et al. Heterozygous deficiency of hypoxia-inducible factor-2alpha protects mice against pulmonary hypertension and right ventricular dysfunction during prolonged hypoxia. *J Clin Invest*. 2003;111(10):1519–1527.
37. Colin F, et al. Mammalian frataxin controls sulfur production and iron entry during de novo Fe4S4 cluster assembly. *J Am Chem Soc*. 2013;135(2):733–740.
38. Bridwell-Rabb J, et al. Human frataxin activates Fe-S cluster biosynthesis by facilitating sulfur transfer chemistry. *Biochemistry*. 2014;53(30):4904–4913.
39. Oktay Y, et al. Hypoxia-inducible factor 2alpha regulates expression of the mitochondrial aconitase chaperone protein frataxin. *J Biol Chem*. 2007;282(16):11750–11756.
40. Nanayakkara G, et al. Cardioprotective HIF-1α-frataxin signaling against ischemia-reperfusion injury. *Am J Physiol Heart Circ Physiol*. 2015;309(5):H867–H879.
41. Ferecatu I, et al. Dysfunction in the mitochondrial Fe-S assembly machinery leads to formation of the chemoresistant truncated VDAC1 isoform without HIF-1α activation. *PLoS One*. 2018;13(3):e0194782.
42. Campuzano V, et al. Frataxin is reduced in Friedreich ataxia patients and is associated with mitochondrial membranes. *Hum Mol Genet*. 1997;6(11):1771–1780.
43. Pandolfo M. Friedreich ataxia: the clinical picture. *J Neurol*. 2009;256(Suppl 1):3–8.
44. Tsou AY, et al. Mortality in Friedreich ataxia. *J Neurol Sci*. 2011;307(1–2):46–49.
45. James TN, Fisch C. Observations on the cardiovascular involvement in Friedreich's ataxia. *Am Heart J*. 1963;66:164–175.
46. Ong KC, et al. Pulmonary hypertension is associated with worse survival in hypertrophic cardiomyopathy. *Eur Heart J Cardiovasc Imaging*.

2016;17(6):604–610.
47. Covella M, et al. Mechanism of progressive heart failure and significance of pulmonary hypertension in obstructive hypertrophic cardiomyopathy. *Circ Heart Fail*. 2017;10(4):e003689.
48. Payne RM. The heart in Friedreich's ataxia: basic findings and clinical implications. *Prog Pediatr Cardiol*. 2011;31(2):103–109.
49. Hanson E, et al. Heart disease in Friedreich's ataxia. *World J Cardiol*. 2019;11(1):1–12.
50. Karthikeyan G, et al. The mitochondrial protein frataxin prevents nuclear damage. *Hum Mol Genet*. 2002;11(11):1351–1362.
51. Haugen AC, et al. Altered gene expression and DNA damage in peripheral blood cells from Friedreich's ataxia patients: cellular model of pathology. *PLoS Genet*. 2010;6(1):e1000812.
52. Igoillo-Esteve M, et al. Unveiling a common mechanism of apoptosis in β-cells and neurons in Friedreich's ataxia. *Hum Mol Genet*. 2015;24(8):2274–2286.
53. Bolinches-Amoros A, et al. Mitochondrial dysfunction induced by frataxin deficiency is associated with cellular senescence and abnormal calcium metabolism. *Front Cell Neurosci*. 2014;8:124.
54. Gomez-Arroyo JG, et al. The monocrotaline model of pulmonary hypertension in perspective. *Am J Physiol Lung Cell Mol Physiol*. 2012;302(4):L363–L369.
55. Steiner MK, et al. Interleukin-6 overexpression induces pulmonary hypertension. *Circ Res*. 2009;104(2):236–244.
56. Lai YC, et al. SIRT3-AMP-activated protein kinase activation by nitrite and metformin improves hyperglycemia and normalizes pulmonary hypertension associated with heart failure with preserved ejection fraction. *Circulation*. 2016;133(8):717–731.
57. Saygin D, et al. Transcriptional profiling of lung cell populations in idiopathic pulmonary arterial hypertension. *Pulm Circ*. https://doi.org/10.1177/2045894020908782.
58. Humbert M, et al. Increased interleukin-1 and interleukin-6 serum concentrations in severe primary pulmonary hypertension. *Am J Respir Crit Care Med*. 1995;151(5):1628–1631.
59. Rabinovitch M, et al. Inflammation and immunity in the pathogenesis of pulmonary arterial hypertension. *Circ Res*. 2014;115(1):165–175.
60. Yuan Y, et al. Cobalt inhibits the interaction between hypoxia-inducible factor-alpha and von Hippel-Lindau protein by direct binding to hypoxia-inducible factor-alpha. *J Biol Chem*. 2003;278(18):15911–15916.
61. Wyszynski RW, et al. Interleukin-1 beta induces the expression and production of stem cell factor by epithelial cells: crucial involvement of the PI-3K/mTOR pathway and HIF-1 transcription complex. *Cell Mol Immunol*. 2016;13(1):47–56.
62. McGettrick AF, O'Neill LAJ. The role of HIF in immunity and inflammation. *Cell Metab*. 2020;32(4):524–536.
63. De Biase I, et al. Epigenetic silencing in Friedreich ataxia is associated with depletion of CTCF (CCCTC-binding factor) and antisense transcription. *PLoS One*. 2009;4(11):e7914.
64. Huang da W, et al. Systematic and integrative analysis of large gene lists using DAVID bioinformatics resources. *Nat Protoc*. 2009;4(1):44–57.
65. Huang da W, et al. Bioinformatics enrichment tools: paths toward the comprehensive functional analysis of large gene lists. *Nucleic Acids Res*. 2009;37(1):1–13.
66. Zhang Y, et al. Conserved electron donor complex Dre2-Tah18 is required for ribonucleotide reductase metallocofactor assembly and DNA synthesis. *Proc Natl Acad Sci U S A*. 2014;111(17):E1695–E1704.
67. Chang J, et al. Clearance of senescent cells by ABT263 rejuvenates aged hematopoietic stem cells in mice. *Nat Med*. 2016;22(1):78–83.
68. Ku S, et al. Friedreich's ataxia induced pluripotent stem cells model intergenerational GAA·TTC triplet repeat instability. *Cell Stem Cell*. 2010;7(5):631–637.
69. Gu M, et al. Patient-specific iPSC-derived endothelial cells uncover pathways that protect against pulmonary hypertension in BMPR2 mutation carriers. *Cell Stem Cell*. 2017;20(4):490–504.e5.
70. Netz DJA, et al. Eukaryotic DNA polymerases require an iron-sulfur cluster for the formation of active complexes. *Nat Chem Biol*. 2012;8(1):125–132.
71. Wang Y, et al. Ephrin-B2 controls VEGF-induced angiogenesis and lymphangiogenesis. *Nature*. 2010;465(7297):483–486.
72. Puccio H, et al. Mouse models for Friedreich ataxia exhibit cardiomyopathy, sensory nerve defect and Fe-S enzyme deficiency followed by intramitochondrial iron deposits. *Nat Genet*. 2001;27(2):181–186.
73. Wirth A, et al. G12-G13-LARG-mediated signaling in vascular smooth muscle is required for salt-induced hypertension. *Nat Med*. 2008;14(1):64–68.
74. Dahlman JE, et al. In vivo endothelial siRNA delivery using polymeric nanoparticles with low molecular weight. *Nat Nanotechnol*. 2014;9(8):648–655.
75. Ortiz-Montero P, et al. Senescence-associated IL-6 and IL-8 cytokines induce a self- and cross-reinforced senescence/inflammatory milieu strengthening tumorigenic capabilities in the MCF-7 breast cancer cell line. *Cell Commun Signal*. 2017;15(1):17.
76. Ast T, et al. Hypoxia rescues frataxin loss by restoring iron sulfur cluster biogenesis. *Cell*. 2019;177(6):1507–1521.
77. Favaro E, et al. MicroRNA-210 regulates mitochondrial free radical response to hypoxia and krebs cycle in cancer cells by targeting iron sulfur cluster protein ISCU. *PLoS One*. 2010;5(4):e10345.
78. Maya-Mendoza A, et al. High speed of fork progression induces DNA replication stress and genomic instability. *Nature*. 2018;559(7713):279–284.
79. Davidson MB, et al. Endogenous DNA replication stress results in expansion of dNTP pools and a mutator phenotype. *EMBO J*. 2012;31(4):895–907.
80. Sanvisens N, et al. Regulation of ribonucleotide reductase in response to iron deficiency. *Mol Cell*. 2011;44(5):759–769.
81. Aird KM, et al. Suppression of nucleotide metabolism underlies the establishment and maintenance of oncogene-induced senescence. *Cell Rep*. 2013;3(4):1252–1265.
82. Shackelford RE, et al. Oxidative stress and cell cycle checkpoint function. *Free Radic Biol Med*. 2000;28(9):1387–1404.
83. Wiley CD, et al. Mitochondrial dysfunction induces senescence with a distinct secretory phenotype. *Cell Metab*. 2016;23(2):303–314.
84. Soon E, et al. Elevated levels of inflammatory cytokines predict survival in idiopathic and familial pulmonary arterial hypertension. *Circulation*. 2010;122(9):920–927.
85. Heresi GA, et al. Plasma interleukin-6 adds prognostic information in pulmonary arterial hypertension. *Eur Respir J*. 2014;43(3):912–914.
86. Cracowski JL, et al. Proinflammatory cytokine levels are linked to death in pulmonary arterial hypertension. *Eur Respir J*. 2014;43(3):915–917.
87. Naeije R, et al. Hemodynamic phenotyping of pulmonary hypertension in left heart failure. *Circ Heart Fail*. 2017;10(9):e004082.
88. Lai YC, et al. Insights into the pulmonary vascular complications of heart failure with preserved ejection fraction. *J Physiol*. 2019;597(4):1143–1156.
89. Kane GC, et al. Impact of age on pulmonary artery systolic pressures at rest and with exercise. *Echo Res Pract*. 2016;3(2):53–61.
90. Baker DJ, et al. Clearance of p16Ink4a-positive senescent cells delays ageing-associated disorders. *Nature*. 2011;479(7372):232–236.
91. Baker DJ, et al. Naturally occurring p16(Ink4a)-positive cells shorten healthy lifespan. *Nature*. 2016;530(7589):184–189.
92. Childs BG, et al. Senescent cells: an emerging target for diseases of ageing. *Nat Rev Drug Discov*. 2017;16(10):718–735.
93. Patro R, et al. Salmon provides fast and bias-aware quantification of transcript expression. *Nat Methods*. 2017;14(4):417–419.
94. Anders S, Huber W. Differential expression analysis for sequence count data. *Genome Biol*. 2010;11(10):R106.